

**Numerical Simulations of Perforated Plate
Stabilized Premixed Flames with Detailed
Chemistry**

by

Kushal Sharad Kedia

M.Tech., B.Tech., Aerospace Engineering,
Indian Institute of Technology Madras (2008)

Submitted to the School of Engineering
in partial fulfillment of the requirements for the degree of
Master of Science in Computation for Design and Optimization
at the

MASSACHUSETTS INSTITUTE OF TECHNOLOGY

June 2010

© Massachusetts Institute of Technology 2010. All rights reserved.

Author
School of Engineering
April 1, 2010

Certified by
Ahmed F. Ghoniem
Professor, Department of Mechanical Engineering
Thesis Supervisor

Accepted by
Karen Wilcox
Associate Professor of Aeronautics and Astronautics
Codirector, Computation for Design and Optimization Program

Numerical Simulations of Perforated Plate Stabilized Premixed Flames with Detailed Chemistry

by

Kushal Sharad Kedia

Submitted to the School of Engineering
on April 1, 2010, in partial fulfillment of the
requirements for the degree of
Master of Science in Computation for Design and Optimization

Abstract

The objective of this work is to develop a high efficiency two-dimensional reactive flow solver to investigate perforated-plate stabilized laminar premixed flames. The developed code is used to examine the impact of the operating conditions and the perforated plate design on the steady flame characteristics. It is also used to numerically investigate the response of these flames to imposed inlet velocity perturbations. The two-dimensional simulations are performed using a reduced chemical kinetics mechanism for methane-air combustion, consisting of 20 species and 79 reactions. Heat exchange is allowed between the gas mixture and the solid plate. The physical model is based on a zero-Mach-number formulation of the axi-symmetric compressible conservation equations.

The steady results suggest that the flame consumption speed, the flame structure, and the flame surface area depend significantly on the equivalence ratio, mean inlet velocity, the distance between the perforated plate holes and the plate thermal conductivity. In the case of an adiabatic plate, a conical flame is formed, anchored near the corner of the hole. When the heat exchange between the mixture and the plate is finite, the flame acquires a Gaussian shape stabilizing at a stand-off distance, that grows with the plate conductivity. The flame tip is negatively curved; i.e. concave with respect to the reactants. Downstream of the plate, the flame base is positively curved; i.e. convex with respect to the reactants, stabilizing above a stagnation region established between neighboring holes. As the plate's thermal conductivity increases, the heat flux to the plate decreases, lowering its top surface temperature. As the equivalence ratio increases, the flame moves closer to the plate, raising its temperature, and lowering the flame stand-off distance. As the mean inlet velocity increases, the flame stabilizes further downstream, the flame tip becomes sharper, hence raising the burning rate at that location. The curvature of the flame base depends on the distance between the neighboring holes; and the flame there is characterized by high concentration of intermediates, like carbon monoxide.

To investigate flame dynamics, linear transfer functions, for low mean inlet velocity oscillations, are analyzed for different equivalence ratio, mean inlet velocity, plate

thermal conductivity and distance between adjacent holes. The oscillations of the heat exchange rate at the top of the burner surface plays a critical role in driving the growth of the perturbations over a wide range of conditions, including resonance. The flame response to the perturbations at its base takes the form of consumption speed oscillations in this region. Flame stand-off distance increases/decreases when the flame-wall interaction strengthens/weakens, impacting the overall dynamics of the heat release. The convective lag between the perturbations and the flame base response govern the phase of heat release rate oscillations. There is an additional convective lag between the perturbations at the flame base and the flame tip which has a weaker impact on the heat release rate oscillations. At higher frequencies, the flame-wall interaction is weaker and the heat release oscillations are driven by the flame area oscillations. The response of the flame to higher amplitude oscillations are used to gain further insight into the mechanisms.

Key words: Laminar premixed flames, perforated-plate stabilized flames, flame-wall interactions, flame consumption speed, stand-off distance.

Thesis Supervisor: Ahmed F. Ghoniem

Title: Professor, Department of Mechanical Engineering

Acknowledgments

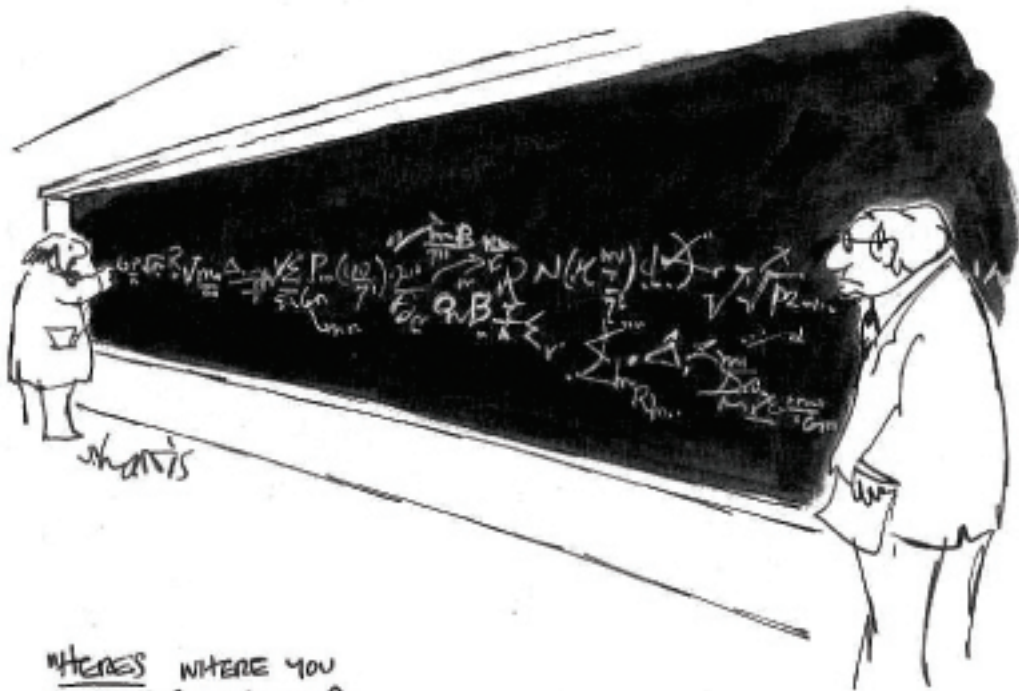
With a deep sense of gratitude, I wish to express my sincere thanks to my research guide, Prof. Ahmed Ghoniem. The confidence and dynamism with which Prof. Ghoniem guided the work requires no elaboration. Profound knowledge and timely wit came as a boon under his guidance.

My sincere thanks are due to Dr. Raymond Speth and Dr. H. Murat Altay for providing me jump start and help me with the scientific arguments and approach. I would also like to thank Dr. Anup Shirgaonkar for helpful discussions and critical comments.

I wish I would never forget the company I had from my fellow research scholars and friends. In particular, I am thankful to Fabrice, Mayank and Won Yong for being great friends and helpful guides in the laboratory. I would like to thank Vainatha for her constant moral support and encouragement. I would also like to mention Sarvee, Vivek, Vibhu, Abishek, Ahmedali, Vikrant, Varun, Sahil, Andrea and the endless list of my friends who have made my life at MIT worth cherishing forever. My thanks are also due to Laura Koller for helping me out with all kinds of administrative issues.

The acknowledgment cannot be complete without thanking my parents Shri. Sharad Kedia and Smt. Meena Kedia, who taught me the value of hard work by their own example and showered upon me their constant blessings. I would like to share this moment of happiness with my beloved sister Ashita, my brother-in-law Sahil, my cousins Pratik and Ankit and my friend Preeti. They rendered me enormous support during the whole tenure of my research.

This work has been sponsored by King Abdullah University of Science and Technology, KAUST, Award No. KUS-I1-010-01.



HERE'S WHERE YOU MADE YOUR MISTAKE. ^

Contents

| | |
|---|-----------|
| Abstract | 4 |
| Acknowledgments | 5 |
| 1 Introduction | 17 |
| 1.1 Thesis Goals | 21 |
| 2 Formulation | 23 |
| 2.1 Governing Equations | 23 |
| 2.2 Boundary Conditions | 25 |
| 2.3 Numerical Methodology | 26 |
| 2.4 Chemical Kinetics Mechanism | 28 |
| 2.5 Validation | 35 |
| 2.6 Summary | 38 |
| 3 Steady Flame Characteristics | 41 |
| 3.1 Effect of the plate thermal conductivity | 41 |
| 3.2 Effect of the equivalence ratio | 51 |
| 3.3 Effect of the mean inlet velocity | 56 |
| 3.4 Effect of distance between two adjacent holes | 58 |
| 3.5 Single-Step Chemical Kinetics | 61 |
| 3.6 Conclusions | 62 |
| 4 Flame Dynamics | 65 |

| | | |
|----------|--|-----------|
| 4.1 | Linear Transfer Functions | 65 |
| 4.2 | Time Domain Analysis | 73 |
| 4.3 | Conclusions | 78 |
| 5 | Summary and Future Work | 79 |
| 5.1 | Summary | 79 |
| 5.2 | Suggested Future Work | 81 |
| | List of Publications based on this thesis | 87 |

List of Figures

| | | |
|-----|--|----|
| 1-1 | A typical perforated-plate burner. Courtesy BOSCH | 17 |
| 2-1 | Schematic of the simulated domain | 26 |
| 2-2 | Boundary conditions | 27 |
| 2-3 | Schematic flowchart of the algorithm based the Najm-Wyckoff fully explicit scheme: NonStiff Scheme (AB2 - second order Adam-Bashforth; CN2 - second order Crank-Nicholson) | 29 |
| 2-4 | Schematic flowchart of the algorithm based the Najm-Wyckoff-Knio semi-implicit stiff scheme: NonSplitStiff Scheme (AB2 - second order Adam-Bashforth; CN2 - second order Crank-Nicholson) | 30 |
| 2-5 | Schematic flowchart of the algorithm based the Najm-Wyckoff-Knio split-semi-implicit-stiff scheme: SplitStiff Scheme (AB2 - second order Adam-Bashforth; RK2 - second order Runge-Kutta) | 31 |
| 2-6 | Performance gain of NonSplitStiff (scheme2) and SplitStiff(scheme3) schemes normalized to the NonStiff(scheme1) scheme. L and M are number of split substeps employed in the momentum diffusion and the species diffusion respectively in the SplitStiff scheme. | 32 |
| 2-7 | Reaction pathway diagram showing the most active carbon species. | 34 |
| 2-8 | (a) The laminar burning velocity; and (b) the flame thickness; as a function of the equivalence ratio calculated using the UCSD mechanism, the reduced mechanism and the GRI-Mech 3.0 mechanism. | 35 |

| | | |
|------|---|----|
| 2-9 | Comparison between the streamwise velocity profiles at different radial locations computed for non-reactive conditions using our 2-D code, and FLUENT. | 37 |
| 2-10 | Comparison between the volumetric heat-release rate profiles in the streamwise direction of the planar disk flame computed using our 2-D code, and the planar unstrained flame computed using our 1-D code [26, 45]. | 38 |
| 2-11 | Grid convergence of the SplitStiff code. | 39 |
| 2-12 | Temporal convergence of the SplitStiff code. | 39 |
| 2-13 | Splitting errors of the SplitStiff code. | 40 |
| 3-1 | The temperature contours for the case of $\phi = 0.75$, $\bar{u}_{in} = 1.3$ m/s, $\kappa = 2R = 1$ mm, and (a) $\lambda_{fh} = 0$, (b) $\lambda_{fh} = 1.5$ W/mK, and (c) $\lambda_{fh} = 10$ W/mK. | 42 |
| 3-2 | The heat flux from the gas to the perforated-plate top surface and the perforated-plate top surface temperatures; as a function of r/D for the case of $\phi = 0.75$, $\bar{u}_{in} = 1.3$ m/s, $\kappa = 2R = 1$ mm, and $\lambda_{fh} = 1.5$ W/mK, and $\lambda_{fh} = 10$ W/mK. | 44 |
| 3-3 | The heat flux from the perforated-plate side surface to the gas as a function of z/D for the case of $\phi = 0.75$, $\bar{u}_{in} = 1.3$ m/s, $\kappa = 2R = 1$ mm, and $\lambda_{fh} = 1.5$ W/mK, and $\lambda_{fh} = 10$ W/mK. | 44 |
| 3-4 | The temperature profile in the radial direction for the case of $\phi = 0.75$, $\bar{u}_{in} = 1.3$ m/s, $\kappa = 2R = 1$ mm, $\lambda_{fh} = 10$ W/mK, at different values of z/D | 45 |
| 3-5 | The fuel mass fraction contours for the case of $\phi = 0.75$, $\bar{u}_{in} = 1.3$ m/s, $\kappa = 2R = 1$ mm, and (a) $\lambda_{fh} = 0$, (b) $\lambda_{fh} = 1.5$ W/mK, and (c) $\lambda_{fh} = 10$ W/mK. | 47 |
| 3-6 | Volumetric heat release rate contours and velocity vectors for the case of $\phi = 0.75$, $\bar{u}_{in} = 1.3$ m/s, $\kappa = 2R = 1$ mm, with (a) $\lambda_{fh} = 0$, (b) $\lambda_{fh} = 1.5$ W/mK, and (c) $\lambda_{fh} = 10$ W/mK. | 48 |

| | | |
|------|--|----|
| 3-7 | The CO mass fraction contours for the case of $\phi = 0.75$, $\bar{u}_{in} = 1.3$ m/s, $\kappa = 2R = 1$ mm, and (a) $\lambda_{fh} = 0$, (b) $\lambda_{fh} = 1.5$ W/mK, and (c) $\lambda_{fh} = 10$ W/mK. | 49 |
| 3-8 | The streamwise velocities along the z direction at $r/D = 0.99$ computed under non-reactive and reactive conditions with different values of λ_{fh} , $\bar{u}_{in} = 1.3$ m/s, $\kappa = 2R = 1$ mm, $\phi = 0.75$ | 50 |
| 3-9 | The temperature contours of steady flames for the case of a conductive perforated-plate, $\lambda_{fh} = 1.5$ W/mK, $\bar{u}_{in} = 1.3$ m/s, $\kappa = 2R = 1$ mm, at (a) $\phi = 0.85$, and (b) $\phi = 0.75$ | 53 |
| 3-10 | The heat flux from the gas to the perforated-plate top surface and the perforated-plate top surface temperature; as a function of r/D at $\phi = 0.85$, and $\phi = 0.75$. $\lambda_{fh} = 1.5$ W/mK, $\bar{u}_{in} = 1.3$ m/s, $\kappa = 2R = 1$ mm | 54 |
| 3-11 | The heat flux from the perforated-plate side surface to the gas as a function of z/D at $\phi = 0.85$, and $\phi = 0.75$. $\lambda_{fh} = 1.5$ W/mK, $\bar{u}_{in} = 1.3$ m/s, $\kappa = 2R = 1$ mm | 54 |
| 3-12 | The contours of the volumetric heat release rate and the velocity vectors for the case of a conductive perforated-plate, $\lambda_{fh} = 1.5$ W/mK, $\bar{u}_{in} = 1.3$ m/s, $\kappa = 2R = 1$ mm, at (a) $\phi = 0.85$, and (b) $\phi = 0.75$ | 55 |
| 3-13 | The contours of the volumetric heat release rate and the velocity vectors for the case of a conductive perforated-plate, $\lambda_{fh} = 1.5$ W/mK, $\phi = 0.75$, $\kappa = 2R = 1$ mm, (a) $\bar{u}_{in} = 0.8$ m/s, and (b) $\bar{u}_{in} = 1.3$ m/s. | 57 |
| 3-14 | The perforated-plate top surface temperatures as a function of r/D for the case of a conductive perforated-plate, $\lambda_{fh} = 1.5$ W/mK, $\phi = 0.75$ m/s, $\kappa = 2R = 1$ mm, at different values of \bar{u}_{in} | 58 |
| 3-15 | The contours of the volumetric heat release rate and the velocity vectors for the case of a conductive perforated-plate, $\lambda_{fh} = 1.5$ W/mK, $\phi = 0.75$, $\bar{u}_{in} = 1.3$ m/s, (a) $\kappa = 2R$, and (b) $\kappa = 3R$ | 59 |

| | | |
|------|--|----|
| 3-16 | The perforated-plate top surface temperatures as a function of r/D for the case of a conductive perforated-plate, $\lambda_{fh} = 1.5$ W/mK, $\phi = 0.75$ m/s, $\bar{u}_{in} = 1.3$ m/s, at different values of κ | 60 |
| 3-17 | The temperature profiles along the centerline for the case of a conductive perforated-plate, $\lambda_{fh} = 1.5$ W/mK, $\phi = 0.75$ m/s, $\bar{u}_{in} = 1.3$ m/s, at different values of κ | 60 |
| 3-18 | Comparison of single-step and multi-step (UCSD reduced) kinetic mechanism simulations, for the case of an adiabatic perforated-plate, $\phi = 0.75$, $\bar{u}_{in} = 0.8$ m/s | 63 |
| 4-1 | Linear flame response: Impact of kinetics mechanism and heat exchange with the plate surface, for constant $\phi = 0.75$, $\bar{u}_{in} = 0.8$ m/s, and $\kappa = 2R = 1$ mm on the total heat release rate, Q_f | 67 |
| 4-2 | Linear flame response: Impact of the mean inlet velocity \bar{u}_{in} , and outer plate radius κ , for constant $\phi = 0.75$ and $\lambda_{fh} = 1.5$ W/mK on the total heat release rate, Q_f | 70 |
| 4-3 | Linear flame response: Impact of the plate thermal conductivity λ_{fh} and equivalence ratio ϕ , for constant $\bar{u}_{in} = 1.3$ m/s and $\kappa = 1$ mm on the total heat release rate, Q_f | 71 |
| 4-4 | Linear response of the heat exchange at the top surface of the plate, Q_{top} , $S_{c,0}$, $S_{c,\kappa}$ and the total heat release rate, Q_f , for $\lambda_f = 1.5$ W/mK, $\phi = 0.75$, $\bar{u}_{in} = 0.8$ m/s, and $\kappa = 2R = 1$ mm | 73 |
| 4-5 | A cycle of Q_f , \bar{u}_{in} , flame area, A_f and Q_{top} for the base case ($\phi = 0.75$, $\lambda_{fh} = 1.5$ W/mK, $\bar{u}_{in} = 1.3$ m/s, $\kappa = 1$ mm) with $A = 0.4$; (a) $f = 50$ Hz and (b) $f = 250$ Hz | 75 |
| 4-6 | A cycle of \bar{u}_{in} , $S_{c,0}$, $S_{c,\kappa}$, and Q_{top} for the base case ($\phi = 0.75$, $\lambda_{fh} = 1.5$ W/mK, $\bar{u}_{in} = 1.3$ m/s, $\kappa = 1$ mm) with $A = 0.4$; (a) $f = 50$ Hz and (b) $f = 250$ Hz | 76 |

4-7 Velocity vectors and volumetric heat release rate contours at different instances of the inlet velocity forcing cycle, with $A = 0.4$, $f = 50$ Hz, $\phi = 0.75$, $\lambda_{fh} = 1.5$ W/mK, $\bar{u}_{in} = 1.3$ m/s, $\kappa = 1$ mm 77

List of Tables

| | | |
|-----|---|----|
| 3.1 | The flame consumption speeds along the centerline, $S_{c,0}$, and along the z direction at $r/D=1$, $S_{c,\kappa}$ at different values of λ_{fh} , $\phi = 0.75$ m/s, $\kappa = 2R = 1$ mm, $\bar{u}_{in} = 1.3$ m/s. The laminar burning velocity of a planar unstretched flame at $\phi = 0.75$ is $S_L = 20.9$ cm/s. | 51 |
| 3.2 | The flame consumption speeds along the centerline and along the z direction at $r/D=1$ for the case of a conductive perforated-plate, $\lambda_{fh} = 1.5$ W/mK, $\bar{u}_{in} = 1.3$ m/s, $\kappa = 2R = 1$ mm, at different values of ϕ . . | 53 |
| 3.3 | The flame consumption speeds along the centerline and along the z direction at $r/D=1$ for the case of a conductive perforated-plate, $\lambda_{fh} = 1.5$ W/mK, $\phi = 0.75$ m/s, $\kappa = 2R = 1$ mm, at different values of \bar{u}_{in} . | 57 |
| 3.4 | The flame consumption speeds along the centerline and along the z direction at $r/D=1.5$ for the case of a conductive perforated-plate, $\lambda_{fh} = 1.5$ W/mK, $\phi = 0.75$ m/s, $\bar{u}_{in} = 1.3$ m/s, at different values of κ . | 61 |
| 3.5 | Summary of the parametric study of steady, laminar perforated-plate stabilized flames in the presence of gas-plate heat exchange. | 64 |

Chapter 1

Introduction

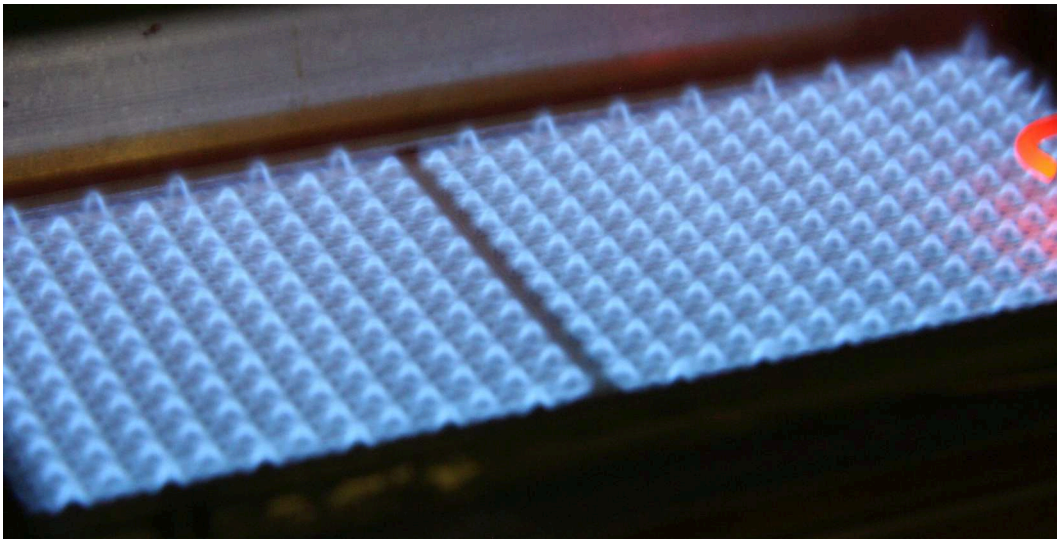


Figure 1-1: A typical perforated-plate burner. Courtesy BOSCH

Perforated-plate stabilized flames are typical in industrial and compact household burners. In these systems several conical premixed flames form downstream of the perforated-plate holes, connected by flames formed downstream of the plate surfaces. The power output is typically low, and the flow is laminar. Figure 1-1 shows a typical perforated-plate burner with premixed flames. The coupling between the acoustics and unsteady heat release rate often leads to self-excited oscillations in such combustion systems. Low emissions, premixed, lean combustion systems are especially prone to thermo-acoustic instabilities (see, e.g., Lieuwen [24], Ducruix et

al. [13], Candel [4] for instability related mechanisms and models). In extreme cases, combustion instabilities may result in flame blowout, flashback, large thermal fluxes through the walls or structural damage. As a result, understanding the impact of thermal properties and the design of the perforated-plate on the steady flame structure and the unsteady flame dynamics is critical.

Durox et al. [14] experimentally investigated the non-linear flame response to acoustic velocity oscillations under different configurations and determined that at certain frequencies, the heat release amplitude is greater than the amplitude of the imposed velocity oscillations. This behavior arises as a result of the thermal interaction between the gases and the plate (flame-wall interaction), which generates significant burning velocity oscillations [31, 29, 30, 40]. Flame-wall interaction forces the flame to anchor at a finite distance away from the plate, defined as the flame stand-off distance. McIntosh and Clarke [32] reviewed models that determine the flame stand-off distance and its temperature. De Goeij and Lange [8] analytically studied the steady, laminar, premixed flame cooling by a burner wall and investigated its impact on the flame thickness and stabilization. Lee and Tsai [23], Daou and Matalon [7], Kim and Maruta [20], and Song et al. [44] numerically analyzed propagating premixed flames in tubes with different thermal and velocity boundary conditions using single-step kinetics mechanism. They explored the flame structure, flame quenching and the extinction for unsteady premixed flames in the presence of flame-wall interactions. McIntosh [31] developed a detailed analytical model for unsteady burner anchored flames assuming single step chemistry while neglecting the oscillations in the flame surface area and taking into account the unsteady heat loss to the burner plate. Rook et al. [38] and Rook [37] also modeled perforated-plate stabilized flame response by solving the uncoupled, one-dimensional, unsteady conservation equations while using the flame surface equation to describe the flame motion. The flame models developed by Rook et al. and McIntosh successfully predict the impact of the oscillatory heat loss to the burner surface. However the predictions are limited by the assumption that the flames are flat, which requires that the mean burning velocity match the mean inlet velocity. Real perforated plate stabilized unsteady flames exhibit flame

area oscillations and curvature effects leading to non-uniform burning velocities along the flame.

An analytical model for the prediction of perforated-plate stabilized flame transfer functions was proposed by Altay et al. [1]. This model incorporates the effects of the two-dimensionality of the flame, the flame area fluctuations and the heat exchange with the plate. However, it relies on specifying of the average flame temperature, and the perforated-plate surface temperature. The mean burning velocity is also assumed to be constant. These assumptions impact the flame transfer function significantly.

Analytical premixed flame models are based on a single-step kinetics mechanism, characterized by an Arrhenius temperature dependence. These analytical models represent the effect of the chemical kinetics processes primarily by the Zeldovich number [6]. This simplification of the complex multi-step chemical kinetics processes captures the physics qualitatively (McIntosh [28], Rook et al. [38] and Rook [37]), but may not agree quantitatively with detailed kinetic mechanism simulations, especially with regards to the flame structure. . Complex multi-step mechanism play an important role in ignition, extinction and flame dynamics. To study these phenomena in detail and understand the underlying mechanisms, it is essential to incorporate a multi-step mechanism in the model. Westbrook and Dryer [46] proposed various single-step mechanisms using curve fitting techniques for methane-air flames. They concluded that none of the single-step mechanisms could accurately describe the chemical structure of the flame, although they could reproduce experimentally observed flammability limits and flame speeds within a certain range of conditions.

Due to limited computational resources, and the complexity of detailed-chemistry combustion models, two-dimensional numerical flame simulations were restricted to single-step chemistry mechanisms or highly reduced chemical mechanisms in the past. Lange and de Goey [10, 11], and Mallens et al. [25] presented numerical analysis of two-dimensional laminar, premixed methane-air flames with single-step chemistry, using adaptive grid refinement techniques. They investigated the impact of different burner geometries and the boundary conditions on the flame shape, and the flow-field. The feedback mechanism between the acoustic field and the unsteady heat release rate

depends on the flame response to small perturbations and is described by the flame transfer functions. Fleifil et al. [17] derived an analytical model for predicting the linear transfer function of a laminar, premixed, ducted flame using the flame surface kinematics, neglecting volume expansion, heat losses and assuming constant burning velocity. Mehta et al. [33] extended this model by retaining exothermic effects like volume expansion across the ducted flame. Experimental results and analytical models for predicting the laminar flame transfer functions of Bunsen-type flames are also available in [12, 41, 42, 14]. These studies demonstrate the importance of flame area oscillations on the dynamic response for different flame anchoring configurations. Kornilov et al. [22] experimentally investigated the acoustic response of premixed flames in Bunsen burners. They concluded that the flame base oscillations are crucial in determining the acoustic flame response. De Goey et al. [9] numerically investigated the acoustic response of multi-slit Bunsen burners. In the numerical solution, they used a single-step chemistry with parameters tuned to match their experimentally observed methane-air flame characteristics. The normalized gain of the transfer functions was greater than unity near a resonant frequency. This resonance was explained by the coupling between the flame area oscillations and the thermal interaction between the hot combustion gases and burner walls (flame-wall interaction).

All of the previous studies had limitations such as:

- Applicability under limited range of operating conditions
- Single-step chemical kinetics mechanism which often gives good qualitative predictions but unreliable quantitative results.
- One-dimensional planar flame assumption which neglects phenomena such as flame-area oscillations, flame stretching and flame curvature
- Use of conventional and expensive numerical schemes.

One needs to overcome these limitations in order to examine the perforated-plate stabilized flame dynamics in detail and with good accuracy. Understanding the steady

flame characteristics is warranted before attempting to understand the dynamic characteristics of the flame. Employing a numerical scheme with high accuracy and low computational cost is needed for such detailed characterization of steady flames. Increasing modern computing power has made detailed numerical flame simulations within reach. Numerical studies of unsteady two-dimensional flames have been reported by several researchers [16, 34, 35, 21, 2].

1.1 Thesis Goals

Two-dimensional numerical computations to simulate steady, laminar, premixed, perforated-plate stabilized, lean methane-air flames at atmospheric pressure, formed downstream of a single perforated-plate hole are performed. The heat exchange between the gases and the solid plate is accounted for. The impact of the perforated-plate thermal properties and design (conductivity of the perforated-plate material, the distance between adjacent perforated-plate holes) and the operating parameters (equivalence ratio, and the mean inlet velocity) on the steady flame structure and characteristics is investigated. The flame dynamic response to imposed velocity perturbations in the presence of flame-wall interaction is also investigated. A reduced chemical kinetics mechanism for methane combustion with 20 species and 79 reactions is used. The research work presented in this thesis can be broadly divided into three distinct areas:

1. Staged development of the numerical code.
2. Investigating steady flame characteristics
3. Analyzing dynamic flame characteristics

This thesis is organized as follows: The formulation and numerical methodology is presented in Chapter 2. The results and discussions are presented in Chapters 3 and 4 with their respective conclusions. Finally, in Chapter 5, the contributions of this thesis are summarized and future work is suggested.

Chapter 2

Formulation

2.1 Governing Equations

Assumptions

- Two-dimensional, laminar and axi-symmetric flow in radial co-ordinate system
- Zero-Mach number formulation
- Acoustic wave propagation is ignored, the pressure field is , and the pressure field is decomposed into a spatially uniform component $p_o(t)$ and a hydrodynamic component $p(z, r, t)$ which varies in space and time.
- Bulk viscosity is assumed to be zero
- Soret-Dufour effects are ignored
- Body forces are ignored
- Radiative heat exchange is ignored
- The mixture is assumed to follow the perfect gas law, with individual species molecular weights, specific heats, and enthalpies of formation; and the Fickian mass diffusion

Under these assumptions, the mass, momentum and the energy conservation equations are respectively expressed as [19]:

$$\frac{\partial \rho}{\partial t} + \nabla \cdot (\rho \vec{V}) = 0 \quad (2.1)$$

$$\frac{\partial(\rho u)}{\partial t} + \frac{\partial(\rho u^2)}{\partial z} + \frac{1}{r} \frac{\partial(r \rho u v)}{\partial r} = -\frac{\partial p}{\partial z} + \Phi_z \quad (2.2)$$

$$\frac{\partial(\rho v)}{\partial t} + \frac{\partial(\rho v u)}{\partial z} + \frac{1}{r} \frac{\partial(r \rho v^2)}{\partial r} = -\frac{\partial p}{\partial r} + \Phi_r \quad (2.3)$$

$$\rho c_p \left(\frac{\partial T}{\partial t} + \vec{V} \cdot \nabla T \right) = \nabla \cdot (\lambda \nabla T) - \sum_{k=1}^K c_{pk} (\vec{j}_k \cdot \nabla T) - \sum_{k=1}^K h_k \dot{\omega}_k W_k \quad (2.4)$$

where ρ is the mixture density, $\vec{V} = (u, v)$ is the velocity vector in the (z, r) radial co-ordinates, Φ_z and Φ_r are the viscous stress terms, λ is the mixture thermal conductivity, $\vec{j}_k = -\rho \frac{W_k}{\bar{W}} D_{km} \nabla X_k$ is the diffusive mass flux vector, W_k is the molar mass of species k , $\bar{W} = 1/(\sum_{k=1}^K Y_k/W_k)$ is the molar mass of the mixture, D_{km} is the mixture average diffusion coefficient for species k relative to the rest of the multi-component mixture, X_k is the mole fraction of species k , c_{pk} is the specific heat of species k at constant pressure, c_p is the mixture specific heat at constant pressure, h_k is the enthalpy of species k , and $\dot{\omega}_k$ is the molar production rate of species k . The production rate of each species is given by the sum of the contributions of elementary reactions with Arrhenius rates. The K th species (the last species), here N_2 is the dominant component in the mixture, and its mass fraction Y_K is calculated from the identity $\sum_{k=1}^K Y_k \equiv 1$. The conservation equation for the k th species, $k = 1, \dots, K-1$, is written as

$$\frac{\partial(\rho Y_k)}{\partial t} + \nabla \cdot (\rho \vec{V} Y_k) = -(\nabla \cdot \vec{j}_k) + \dot{\omega}_k W_k \quad (2.5)$$

The perfect gas state equation is expressed as

$$p_o = \rho \hat{R}T / \bar{W} \quad (2.6)$$

where \hat{R} is the universal gas constant. Finally, for the purposes of the numerical implementation, the time rate of change of density is found by differentiating the state equation

$$\frac{\partial \rho}{\partial t} = \rho \left(-\frac{1}{T} \frac{\partial T}{\partial t} - \bar{W} \sum_{k=1}^K \frac{1}{W_k} \frac{\partial Y_k}{\partial t} \right) \quad (2.7)$$

where $\partial Y_k / \partial t = [\partial(\rho Y_k) / \partial t + \nabla(\rho \vec{V}) Y_k] / \rho$ and substituting for $\partial T / \partial t$ and $\partial(\rho Y_k) / \partial t$ from the energy and species conservation equations, respectively.

In order to include the effect of the heat exchange with the perforated -plate, the heat conduction equation within the burner plate is solved

$$\rho_{fh} c_{fh} \frac{\partial T}{\partial t} = \nabla \cdot (\lambda_{fh} \nabla T) \quad (2.8)$$

where ρ_{fh} , c_{fh} , and λ_{fh} are the density, specific heat and thermal conductivity of the burner plate material, respectively. For simplicity they are assumed to be constant.

A flame stabilized downstream of a single perforated-plate hole is simulated. The solution domain at the perforated-plate is shown in Fig. 2-1.

2.2 Boundary Conditions

Figure 2-2 shows a schematic diagram of the computational domain at an arbitrary angular slice, illustrating the boundary conditions specified at each surface. The conduction heat exchange between the perforated-plate and the gas mixture is considered. Convective heat transfer is modeled at the bottom surface of the perforated-plate using a constant specified convective heat transfer coefficient, h . The gas temperature at the inlet is assumed to be uniform and at the free stream value. The impact of this boundary condition will be discussed further in the Chapter 3. Symmetry boundary



Figure 2-1: Schematic of the simulated domain

conditions are imposed at the centerline, $r = 0$. Adiabatic, impermeable, slip-wall boundary periodic conditions are used at the right boundary in order to model the interaction between adjacent flames. At the exit, typical out-flow boundary conditions are used. The average inlet velocity, \bar{u}_{in} , is kept constant to simulate steady flames. The mixture composition at the inlet is steady and uniform and calculated based on the specified equivalence ratio of the reactant mixture. The inlet temperature of the gas is uniform and at its value in the environment. The pressure gradient, and the velocity profile at the inlet are calculated based on the the laminar, fully developed flow assumption.

2.3 Numerical Methodology

The conservation equations are solved using a second-order predictor-corrector finite-difference projection scheme. The domain is discretized using a staggered grid with uniform, but different cell sizes in each coordinate direction. Velocity components are evaluated at the cell edges, while scalars are evaluated at the cell centers. Spatial derivatives are discretized using second-order central differences. The equations are integrated using an additive (non-split) semi-implicit second-order projection scheme.

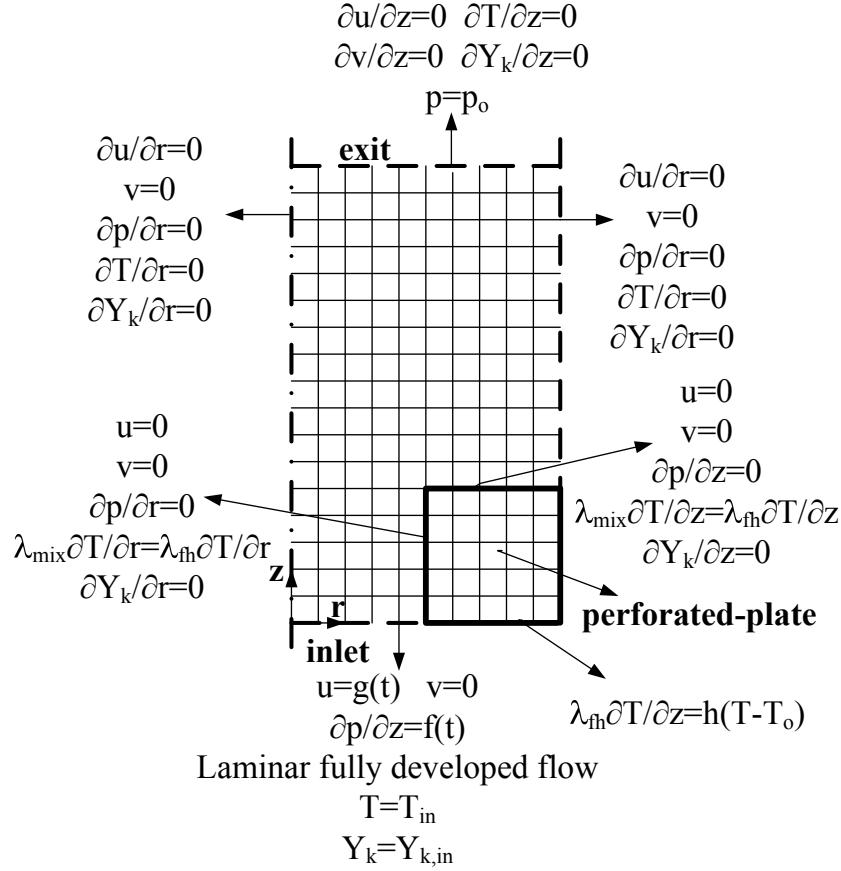


Figure 2-2: Boundary conditions

The projection scheme is based on a predictor-corrector stiff approach that couples the evolution of the velocity and density fields in order to stabilize computations of reacting flows with large density variations. The solver code is developed in three incremental stages, based on the work of Najm et. al. [35] and Knio et. al. [21]. Figures 2-3, 2-4 and 2-5 shows the numerical algorithm implemented in each of the three schemes. The schemes have implementations of a combination of standard second order Runge-Kutta (RK2) and/or second order Adam-Bashforth (AB2) and/or second order Crank-Nicholson (CN2). In all the schemes there is a pressure correction step which involves the inversion of the pressure Poisson equation which is implemented using Sundials banded matrix solver. The stiff integrator is adapted from the CVODE

package [3]. A detailed explanation of these schemes can be found in [35]¹. and [21]².

The calculation of the production rates of each species and the evaluation of the thermodynamic and transport properties are performed using Cantera [18]. The code is developed in C++, and parallelized using OpenMP. A one-dimensional flame solution is used as the initial condition.

Figure 2-6 shows the relative performance of the three schemes. The Nonstiff scheme (scheme 1, Fig. 2-3) has most stringent time step restriction as it is completely explicit scheme. The restriction comes from the stiff chemical kinetics. This can be improved by have stiff integration of the reaction rate terms implicitly and rest all terms explicitly or the NonSplitStiff scheme (scheme2, Fig. 2-4). This scheme now gets restricted by diffusion of very light species such as hydrogen ions. Strang splitting can be implemented in diffusion terms and a SplitStiff scheme (scheme3, Fig. 2-5) is obtained. Moving from Scheme 1 to Scheme 3, there is an additional functional overhead of implicit integration and diffusion splitting which results in diminishing gains. However, significant overall performance gains are stiff observed using Scheme 3, as seen in the figure. A performance gain of 100x can be obtained for a certain combination of Scheme 3 parameters as compared to fully explicit NonStiff scheme 1.

2.4 Chemical Kinetics Mechanism

A reduced methane reaction kinetics mechanism involving 20 species and 79 reactions, which is obtained by eliminating some species and reactions from the mechanism developed by UCSD Center of Energy Research [36], is used. In order to obtain the reduced mechanism, simulations of a premixed laminar flame stabilized in a planar

¹The corrected equations in [35] are:

$$\text{Eq. (31)} \quad C_\rho \equiv \frac{\rho}{T} \left(\mathbf{v} - \frac{1}{c_p \text{ReSc}} \mathbf{Z} \right) \cdot \nabla T$$

$$\text{Eq. (33)} \quad E_\rho \equiv \bar{W} \sum_{i=1}^N \frac{\nabla \cdot (\rho \mathbf{v} Y_i) + (1/\text{ReSc}) \nabla \cdot (\rho Y_i \mathbf{V}_i) - Y_i \nabla \cdot (\rho \mathbf{v})}{W_i}$$

$$\text{Eq. (35)} \quad \varepsilon_\rho \equiv -\bar{W} \sum_{i=1}^N \frac{D a w_i}{W_i}$$

²The corrected equations in [21] are:

$$\text{Eq. (11)} \quad D_\rho = -\frac{1}{\text{Re Pr } c_p T} \nabla \cdot (\lambda \nabla T) - \frac{\rho}{T} \frac{1}{c_p \text{ReSc}} \mathbf{Z} \cdot \nabla T$$

$$\text{Eq. (27)} \quad \left. \frac{\partial \rho}{\partial t} \right|^{**} = \frac{1}{2\Delta t} (3\rho^{n+1} - 4\rho^n + \rho^{n-1})$$

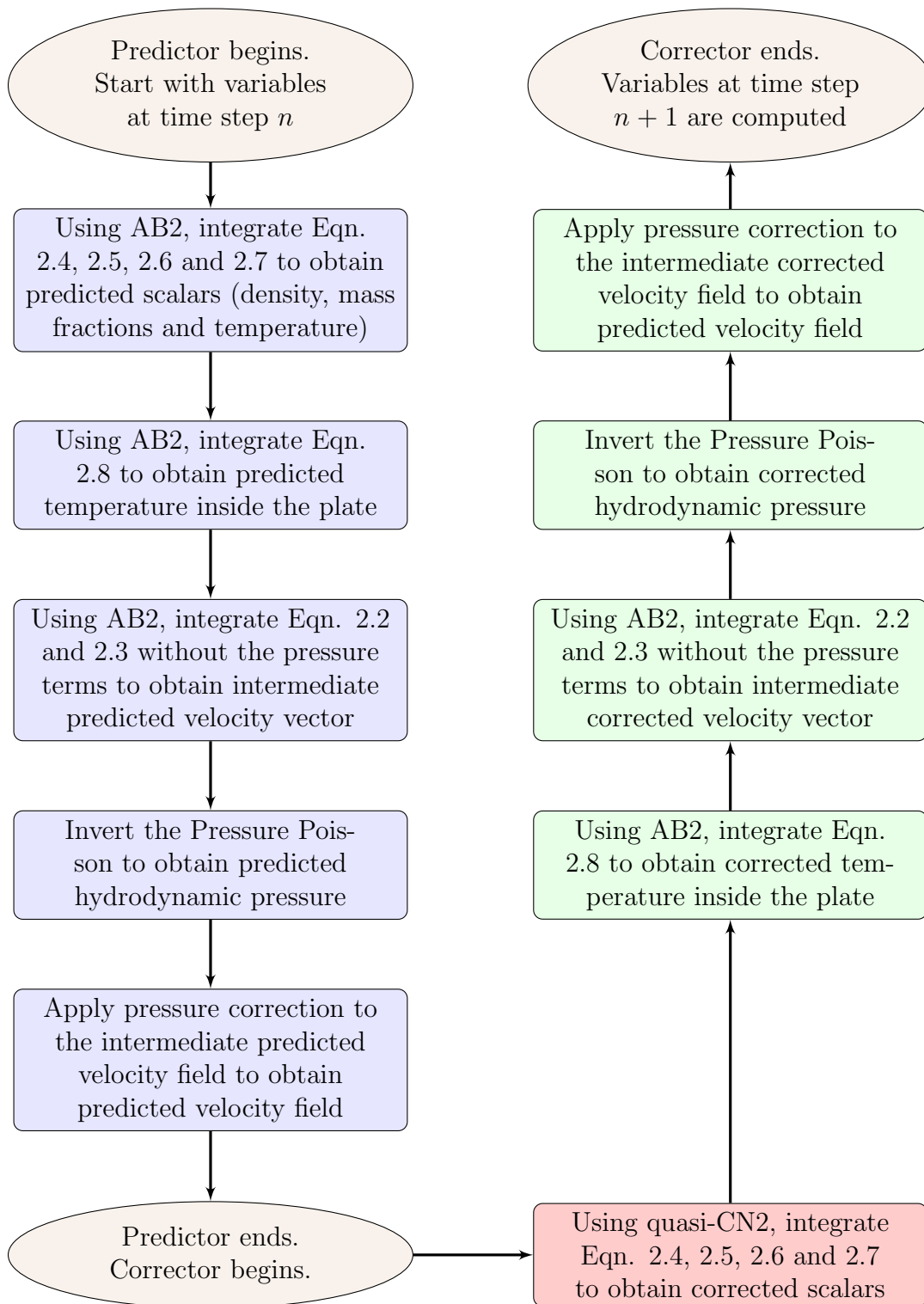


Figure 2-3: Schematic flowchart of the algorithm based the Najm-Wyckoff fully explicit scheme: NonStiff Scheme (AB2 - second order Adam-Bashforth; CN2 - second order Crank-Nicholson)

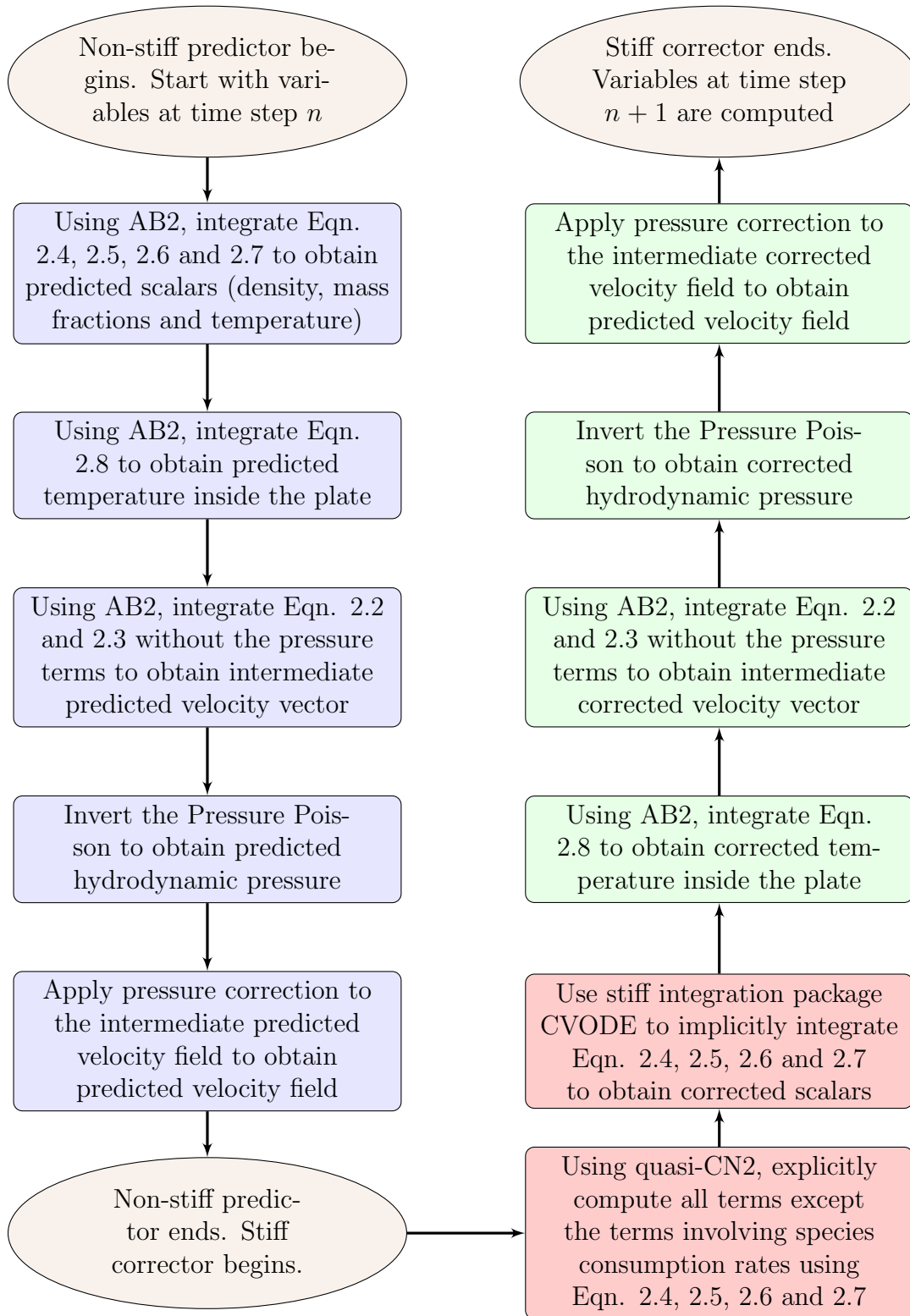


Figure 2-4: Schematic flowchart of the algorithm based the Najm-Wyckoff-Knio semi-implicit stiff scheme: NonSplitStiff Scheme (AB2 - second order Adam-Bashforth; CN2 - second order Crank-Nicholson)

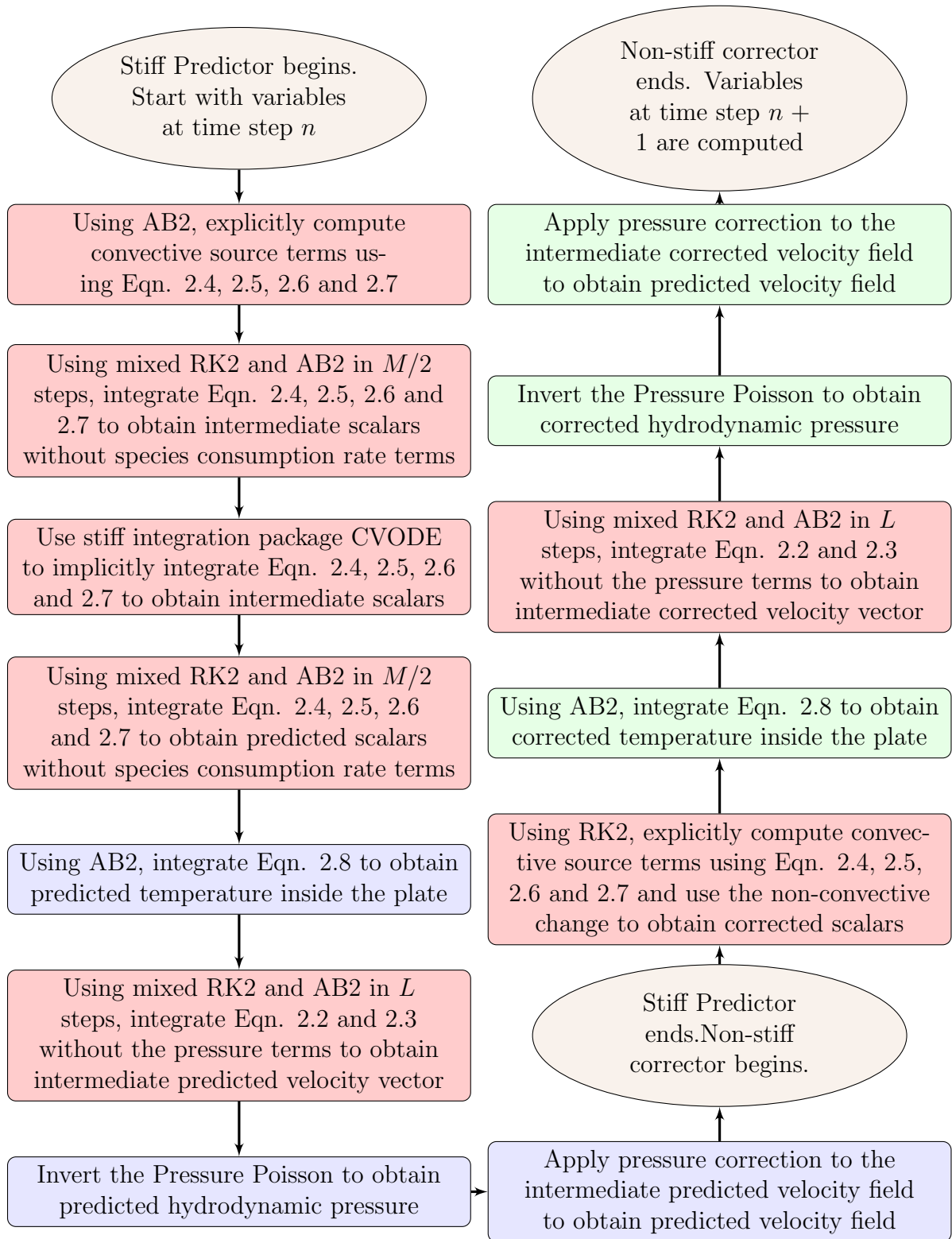


Figure 2-5: Schematic flowchart of the algorithm based the Najm-Wyckoff-Knio split-stiff scheme: SplitStiff Scheme (AB2 - second order Adam-Bashforth; RK2 - second order Runge-Kutta)

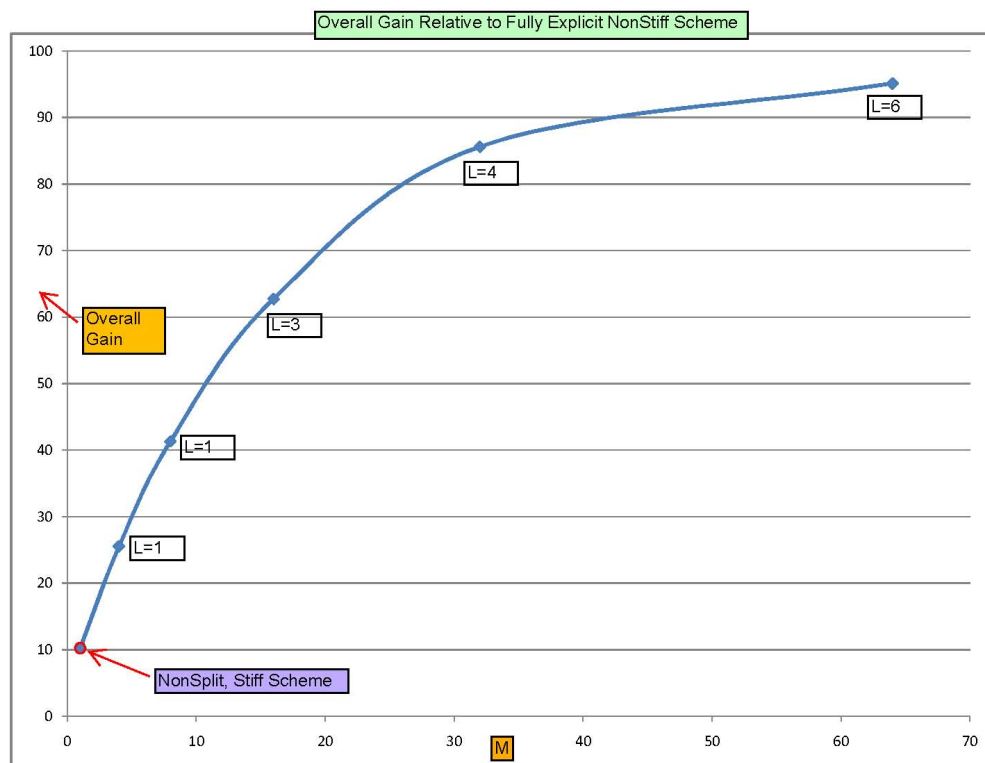


Figure 2-6: Performance gain of NonSplitStiff (scheme2) and SplitStiff(scheme3) schemes normalized to the NonStiff(scheme1) scheme. L and M are number of split substeps employed in the momentum diffusion and the species diffusion respectively in the SplitStiff scheme.

stagnation flow using the one-dimensional code developed in our research group were performed. Reactants are supplied on one side, the equilibrium state products of the reactants are supplied on the other, and the flame stabilizes in the vicinity of the stagnation point. The corresponding potential flow velocity field is characterized by the time-varying strain rate parameter a . Computations for strain rates ranging from 12 to 9000 s^{-1} were performed. In all cases, the oxidizer was air, the reactant mixture temperature was 300 K, and the pressure was atmospheric. Details of the solution can be found in Refs. [26, 45].

First, the one-dimensional code was run with the full UCSD mechanism. Given a set of elementary reactions that convert species A to species B, the reaction rates for each of these reactions are summed and this value is integrated across the flame, obtaining the total rate at which A is converted to B. One way of displaying this

information is a reaction pathway diagram, which shows the conversion rates amongst the reacting species. Figure 2-7 shows the reaction pathway diagram for a planar methane-air flame with an equivalence ratio of 0.80 and $a = 12 \text{ s}^{-1}$ displaying the most active carbon-containing species obtained using the UCSD mechanism. In this figure, colors and line width are used to indicate the magnitude of each conversion rate. Every time the line width in the figure is reduced indicates a halving of the corresponding conversion rate. Conversions which occur at rates of less than 1% of the rate at which methane is consumed, and the carbon containing species involved in these conversions are not shown. Based on this figure, it is observed that the contribution of the species at the right-side branch (starting from the CH_3 recombination reaction) are not significant compared to the other major reaction pathways. Therefore, only the following species (and the reactions involving those species) were retained in the reduced chemical kinetics mechanism: N_2 , H , O_2 , OH , O , H_2 , H_2O , HO_2 , H_2O_2 , CO , CO_2 , HCO , CH_2O , CH_4 , CH_3 , T-CH_2 , S-CH_2 , CH_3O , CH_2OH , and CH_3OH .

In order to test the validity of the reduced mechanism, the burning velocities and the flame thicknesses calculated using the full UCSD mechanism, the reduced mechanism, as well as the commonly used GRI-Mech 3.0 mechanism [43] are compared. The consumption speed, S_c , is used to quantify the burning velocity. The consumption speed is calculated by integrating the energy equation across the flame. The consumption speed is defined as

$$S_c = \frac{\int_{-\infty}^{\infty} q''' / c_p dy}{\rho_u (T_b - T_u)} \quad (2.9)$$

where q''' is the volumetric heat release rate, c_p is the specific heat of the mixture, y is the coordinate normal to the flame, ρ_u is the unburned mixture density, T_u and T_b are the unburned and burned temperature, respectively, and y is the normal to the flame or the normal to the constant temperature contours. In this thesis, S_c is evaluated along the centerline ($r/D = 0$) and along the edge of the simulated domain ($r/D = \kappa$). As the strain rate parameter a approaches 0, the consumption speed approaches the laminar burning velocity.

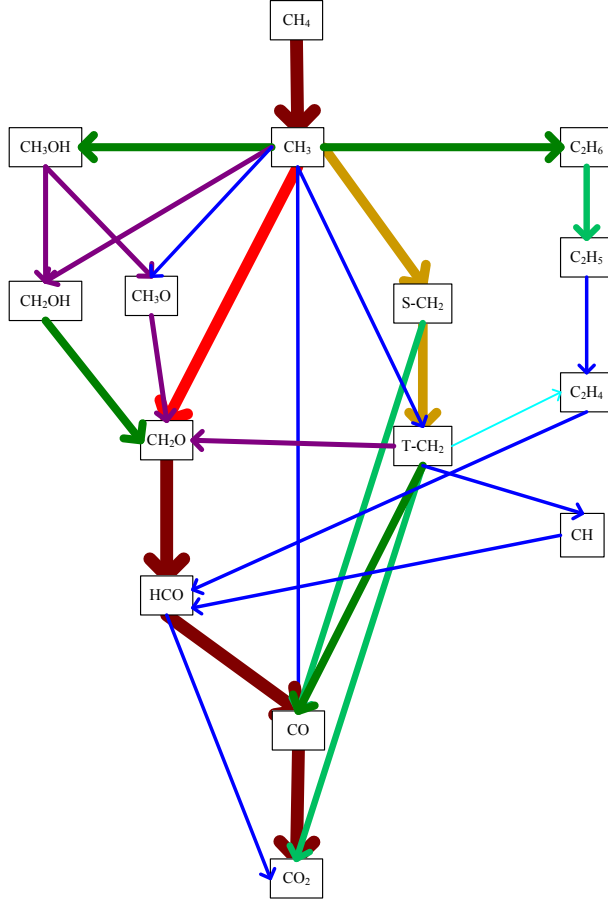


Figure 2-7: Reaction pathway diagram showing the most active carbon species.

The flame thickness is determined using the peak temperature gradient and the unburned and burned temperatures as follows

$$\delta_f = (T_b - T_u) / |\partial T / \partial x|_{max} \quad (2.10)$$

The laminar burning velocity, i.e. at $a = 0$, as a function of the equivalence ratio using the UCSD mechanism, the reduced mechanism and the GRI-Mech 3.0 mechanism is shown in Fig. 2-8a. The laminar burning velocity is determined by extrapolating the consumption speed to a strain rate of zero, analogous to the commonly-employed technique for determining laminar burning velocity from experimentally-observed strained flames. Figure 2-8b shows the flame thickness as a function of the equivalence ratio calculated for a strain rate of $a = 48 \text{ s}^{-1}$, using the three kinetics mechanisms.

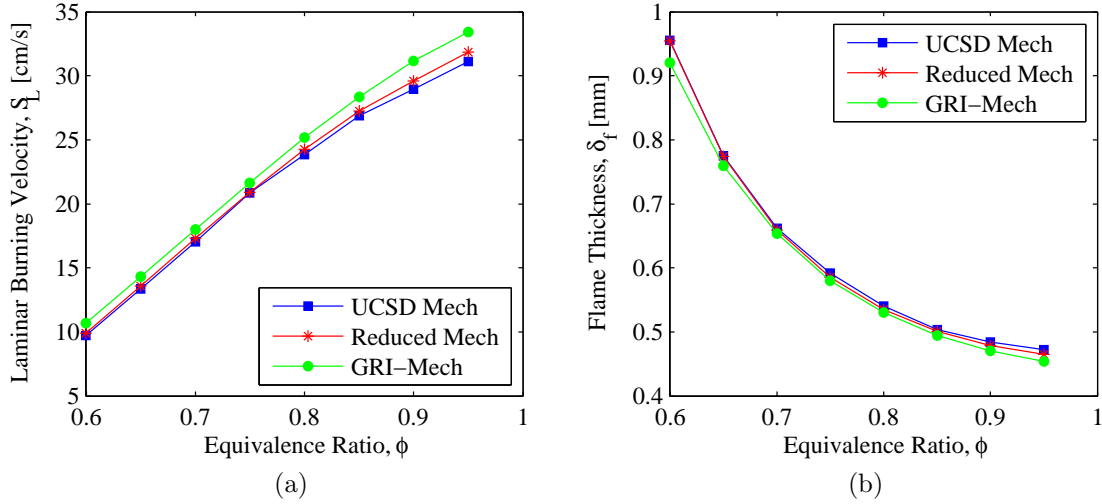


Figure 2-8: (a) The laminar burning velocity; and (b) the flame thickness; as a function of the equivalence ratio calculated using the UCSD mechanism, the reduced mechanism and the GRI-Mech 3.0 mechanism.

Figure 2-8 shows that in the lean equivalence ratio range, both the laminar burning velocity and the flame thickness are well predicted with the reduced mechanism. The laminar burning velocities calculated with the UCSD mechanism (and the reduced mechanism) are lower than those calculated by the GRI-Mech mechanism, and the difference between the calculated burning velocities increases as the equivalence ratio approaches stoichiometry. This study is restricted to the lean equivalence ratio regime. Thus the use of the reduced mechanism seems justified.

2.5 Validation

The two-dimensional reactive code used in this study is validated by comparing (i) the computed velocity profiles under non-reactive conditions with those computed with the commercial flow solver FLUENT using the same grid resolution, operating conditions and the domain dimensions, and (ii) the volumetric heat-release rate profile computed in the absence of the plate, simulating a planar, unstretched disk flame with that computed by the one-dimensional code described above simulating a planar, unstrained flame ($a = 0$) at equivalence ratio of $\phi = 0.75$, using the reduced

mechanism in both codes. For the non-reactive validation, the operating conditions, the grid resolution and the domain dimensions were selected as follows: The non-reactive fluid is a methane-air mixture at 300 K with $\phi = 0.75$; the average inlet velocity, $\bar{u}_{in}=1.3$ m/s; the radius of the hole, $R = 0.5$ mm; half the distance between two adjacent holes (the radius of the simulation domain), $\kappa = 2R$; the plate thickness (the distance from the inlet to the top of the plate), $t = 13.2$ mm; the distance between the top surface of the plate and the exit of the domain, $L_d=15$ mm; the cell size in the streamwise direction, $\Delta z = 0.04$ mm; the cell size in the radial direction, $\Delta r = 0.02$ mm.

The computed streamwise velocity profiles under non-reactive conditions, at two different radial locations are compared in Fig. 2-9. The velocity profiles computed with our code match with those computed with FLUENT. The volumetric heat-release rate profile along the streamwise direction of the two-dimensional disk flame match very well with that of the one-dimensional, planar, unstrained flame as shown in Fig. 2-10. The flame temperature, and consumption speeds were also verified to be the same. These results demonstrate the accuracy of our two-dimensional reactive code.

SplitStiff code validation

The validation of the SplitStiff code is presented in this section. M is the number of substeps implemented in the species diffusion terms integration and L is the number of substeps implemented in the momentum diffusion terms integration. Figure 2-11 shows the grid convergence analysis. The RMS errors are relative to the finest grid with $dz = 20 \mu\text{m}$. As expected the errors increase with an increase in the grid size. The global CFL dt/dz^2 is kept constant while increasing the grid resolution. M and L are kept constant. Figure 2-12 shows the temporal convergence analysis. The RMS errors are relative to the smallest time step $dt = 40$ ns. M and L are kept constant. The total time for simulating an unsteady flow was kept constant while changing the global step size. The accuracy decreases as the time step increases. Both the grid convergence and temporal convergence analysis show that the scheme is second order in time and space.

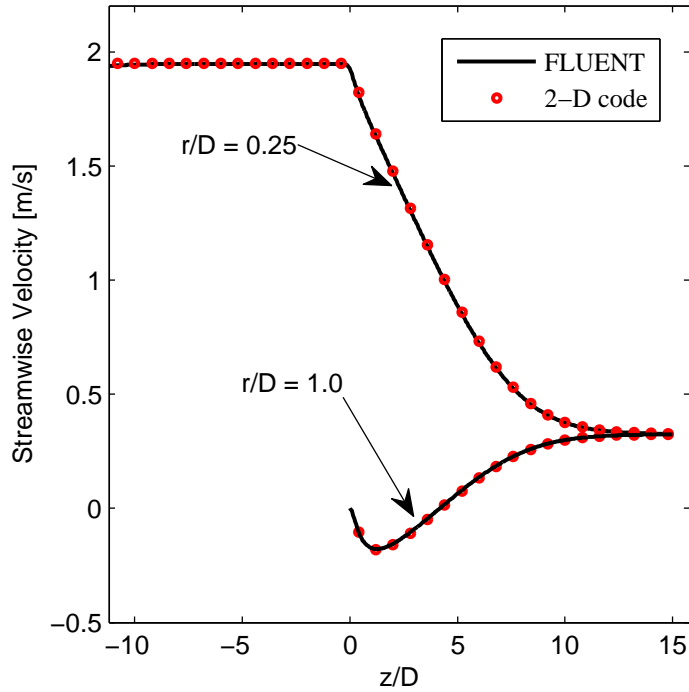


Figure 2-9: Comparison between the streamwise velocity profiles at different radial locations computed for non-reactive conditions using our 2-D code, and FLUENT.

Figure 2-13 shows the errors occurring due to splitting. The global time step dt is kept constant. RMS errors are relative to the NonSplitStiff scheme. With increasing species diffusion splitting (M), it is seen that the RMS errors do not show significant change. Hence higher M can be used to improve the overall stable time step, keeping in mind the diminishing gains as seen before.

Analysis of the numerical implementation suggested using SplitStiff simulations for obtaining reactive flow results. All the results presented in the thesis have obtained using SplitStiff scheme with $M=32$, $L=4$, global $dt = 800$ ns. The cell size in the flow direction is $dz = 40 \mu\text{m}$ and the cell size in the radial direction is $dr = 20 \mu\text{m}$. The simulations were performed on a 2.66GHz CPU speed Intel Xeon - Harpertown node consisting of dual quad-core CPUs (8 processors).

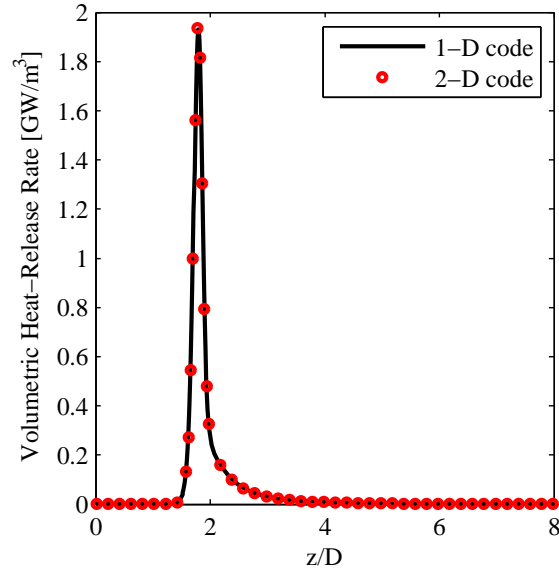


Figure 2-10: Comparison between the volumetric heat-release rate profiles in the streamwise direction of the planar disk flame computed using our 2-D code, and the planar unstrained flame computed using our 1-D code [26, 45].

2.6 Summary

In this chapter, the governing equations and boundary conditions are described. Numerical solution with schematic implementation procedure along with a complete code validation is presented. The detailed chemical kinetics mechanism used is also described. Analyzing different schemes, it was inferred that the SplitStiff scheme is highly efficient. An optimal set of parameters (splitting, time step and grid size) for the SplitStiff code were identified for using it for improving the performance of the code without losing accuracy of the computations. In the next chapters, various results using the developed code are discussed.

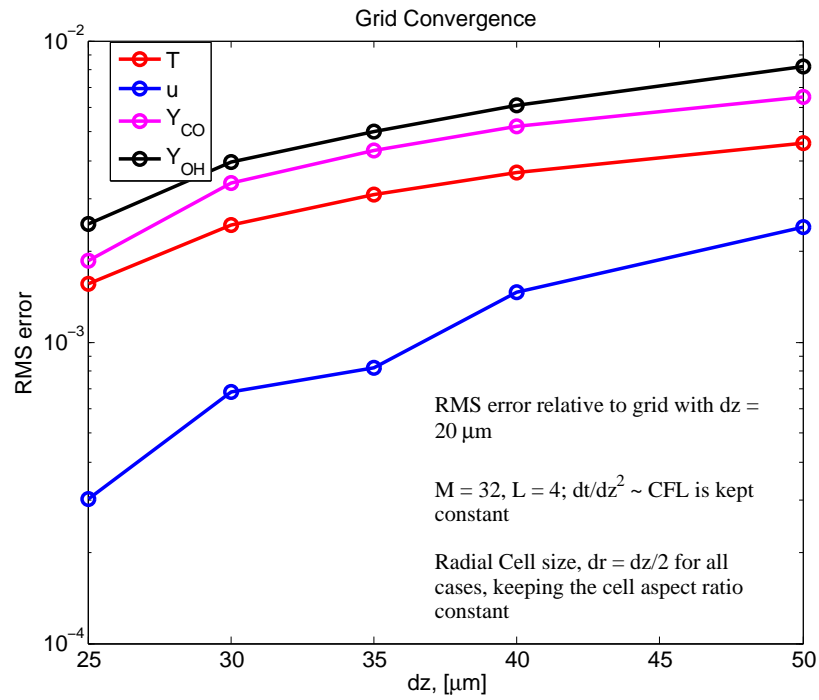


Figure 2-11: Grid convergence of the SplitStiff code.

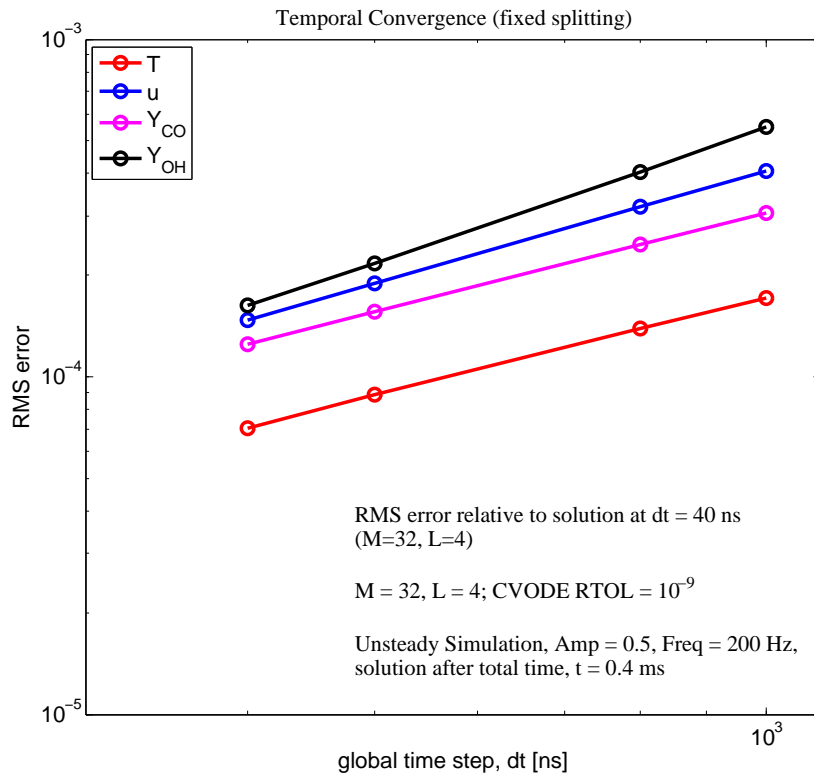


Figure 2-12: Temporal convergence of the SplitStiff code.

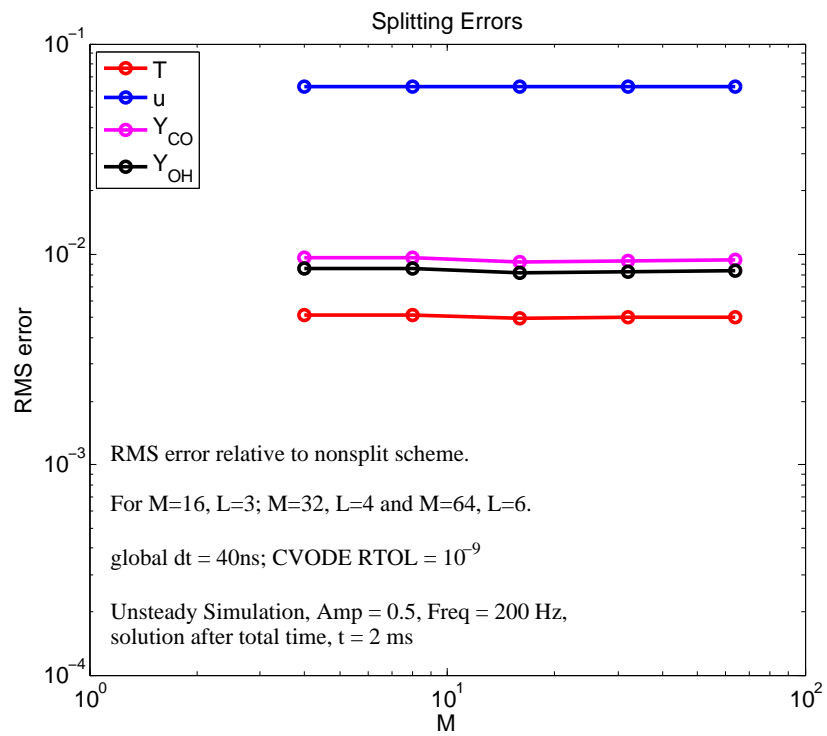


Figure 2-13: Splitting errors of the SplitStiff code.

Chapter 3

Steady Flame Characteristics

In this chapter, the steady flame characteristics are investigated under different operating conditions, perforated-plate thermal properties and designs. The equivalence ratio, ϕ ; the average inlet velocity, \bar{u}_{in} , the thermal conductivity of the perforated-plate material, λ_{fh} , and half the distance between two adjacent holes (the radius of the simulation domain), κ , are varied to perform a detailed parametric study. The following parameters are kept constant: the radius of the hole, $R = 0.5$ mm; the plate thickness, $t = 13.2$ mm; the distance between the top surface of the plate and the exit of the domain, $L_d = 15$ mm; the inlet temperature, $T_{in} = 300$ K; the inlet Prandtl number of the mixture, $Pr = 0.71$; $\rho_{fh} = 2400$ kg/m³; $c_{fh} = 1070$ J/kgK.

3.1 Effect of the plate thermal conductivity

First, the impact of the plate conductivity on the steady flame characteristics are investigated. I performed the simulations with $\lambda_{fh} = 0$ (no gas-plate heat exchange), $\lambda_{fh} = 1.5$ W/mK and $\lambda_{fh} = 10$ W/mK, while keeping the other parameters constant at $\phi = 0.75$, $\bar{u}_{in} = 1.3$ m/s, and $\kappa = 2R = 1$ mm. The corresponding Zeldovich number, $Ze = \frac{E_a}{RT_b^2}(T_b - T_u)$ is $Ze = 10.7$ (assuming $\frac{E_a}{R} = 24400$ K) and the inlet Reynolds number based on the maximum velocity and hole diameter is $Re = 162$. For the plate, the thickness ratio based on the difference between the outer and inner diameter, D_p , and the plate thickness, t is $(t/D_p) = 13.2$.

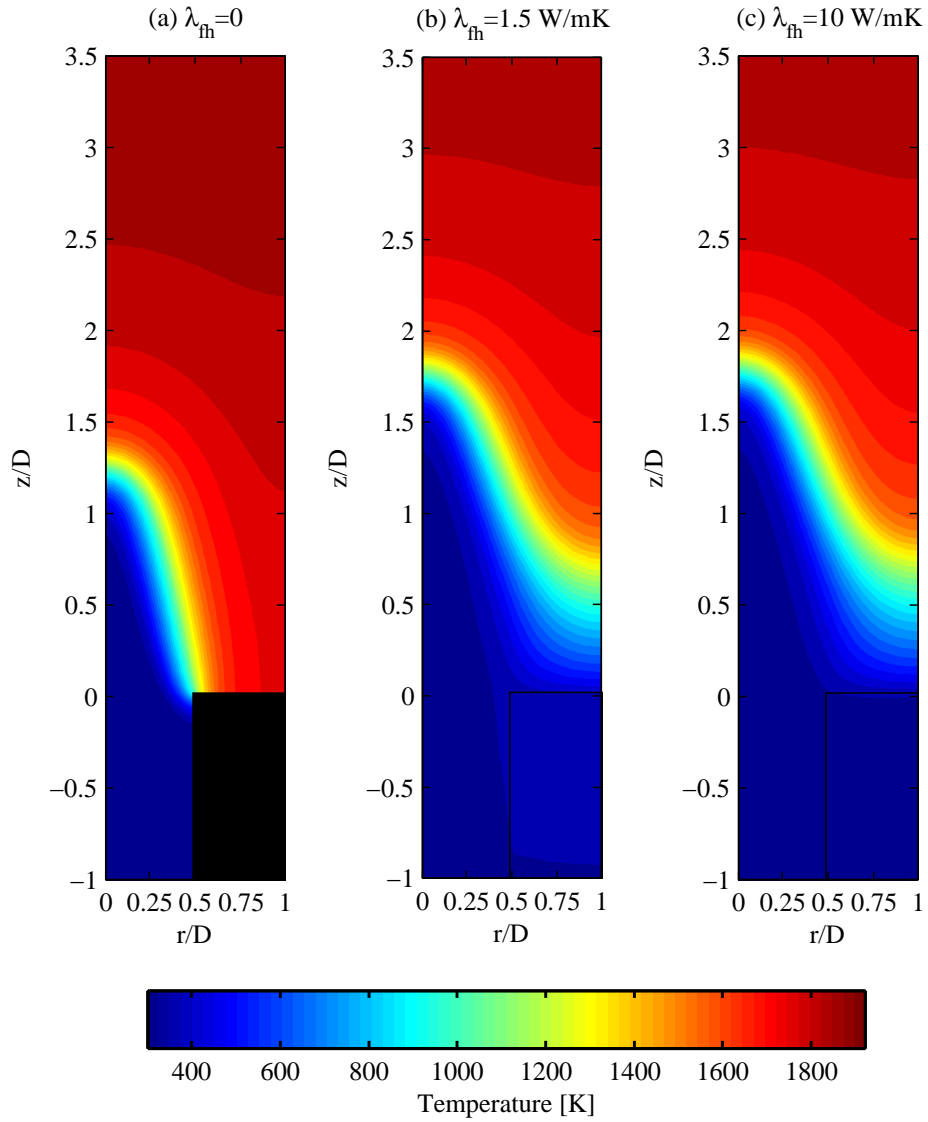


Figure 3-1: The temperature contours for the case of $\phi = 0.75$, $\bar{u}_{in} = 1.3 \text{ m/s}$, $\kappa = 2R = 1 \text{ mm}$, and (a) $\lambda_{fh} = 0$, (b) $\lambda_{fh} = 1.5 \text{ W/mK}$, and (c) $\lambda_{fh} = 10 \text{ W/mK}$.

In Fig. 3-1, the temperature contours at different values of λ_{fh} are shown. The streamwise extent of the domain in the figures is chosen near the flame location, and does not represent the entire computational domain in that direction. When $\lambda_{fh} = 0$ (without heat exchange), a conical flame is anchored near the corner of the perforated-plate. When $\lambda_{fh} > 0$, i.e. with gas-plate heat exchange, the temperature contours are horizontal downstream of the plate surface near the right domain boundary, suggesting that the flame extends to cover the distance between adjacent hole immediately downstream of the plate. The flame above the plate is anchored a finite distance away from the plate; the flame stand-off distance. As λ_{fh} increases, the flame stand-off distance increases. The flame is conical as a result of large flow velocities relative to the laminar burning velocity. The flame angle is such that the normal component of the flow velocity matches the local burning velocity to stabilize the flame. The flow velocities above the plate are very low, i.e., a nearly stagnant zone forms. This zone is referred to as the stagnation zone in this thesis. This, along with the symmetry boundary condition on the right side boundary results in a flame convex towards the reactants (positively curved) in that region, for cases with $\lambda_{fh} > 0$.

Figure 3-2 shows the heat flux from the gas to the top surface of the perforated-plate as a function of the radial coordinate at $\lambda_{fh} = 1.5$ W/mK and $\lambda_{fh} = 10$ W/mK. The heat flux increases along the radial direction, and decreases as λ_{fh} increases. The top surface temperature of the perforated-plate, T_s , as a function of the radial coordinate for the same cases in Fig. 3-2 is plotted ¹. As λ_{fh} increases, T_s decreases as a result of the lower heat transfer rate. The heat flux from the perforated-plate side surface to the gas as a function of the streamwise coordinate is shown in Fig. 3-3. When $\lambda_{fh} = 1.5$ W/mK, the heat flux is largest close to the top surface, and drops to low values near the bottom surface. The temperature of the bottom surface of the plate is close to the ambient temperature, $T_{bot} \simeq 300$ K. When $\lambda_{fh} = 10$

¹The surface temperature of the plate is undefined in the case when conductivity is zero, since the boundary wall acts as an insulating boundary. In this case, there is no flame-wall heat exchange. The temperature on the surface and within the plate, thus, is an artifact of the initial conditions, which does not impact the flow-field.

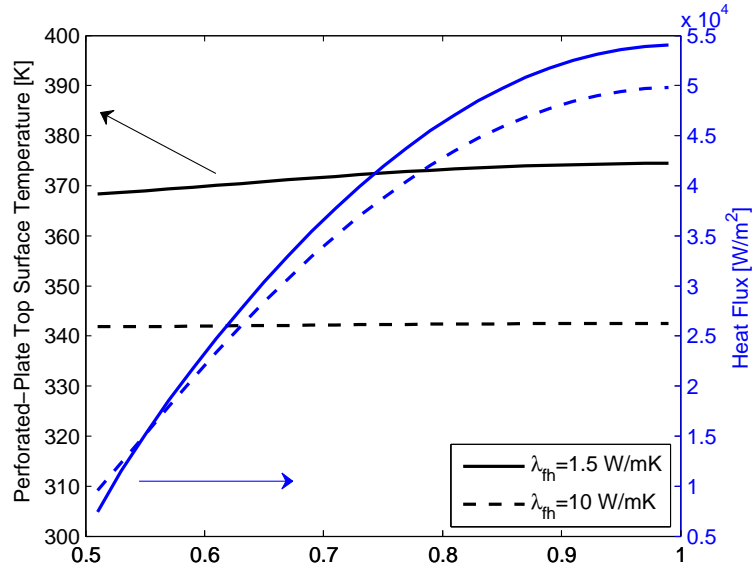


Figure 3-2: The heat flux from the gas to the perforated-plate top surface and the perforated-plate top surface temperatures; as a function of r/D for the case of $\phi = 0.75$, $\bar{u}_{in} = 1.3$ m/s, $\kappa = 2R = 1$ mm, and $\lambda_{fh} = 1.5$ W/mK, and $\lambda_{fh} = 10$ W/mK.

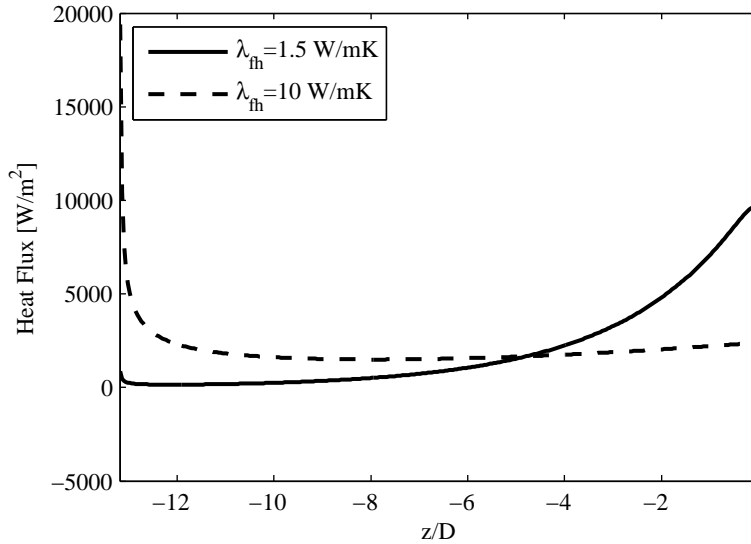


Figure 3-3: The heat flux from the perforated-plate side surface to the gas as a function of z/D for the case of $\phi = 0.75$, $\bar{u}_{in} = 1.3$ m/s, $\kappa = 2R = 1$ mm, and $\lambda_{fh} = 1.5$ W/mK, and $\lambda_{fh} = 10$ W/mK.

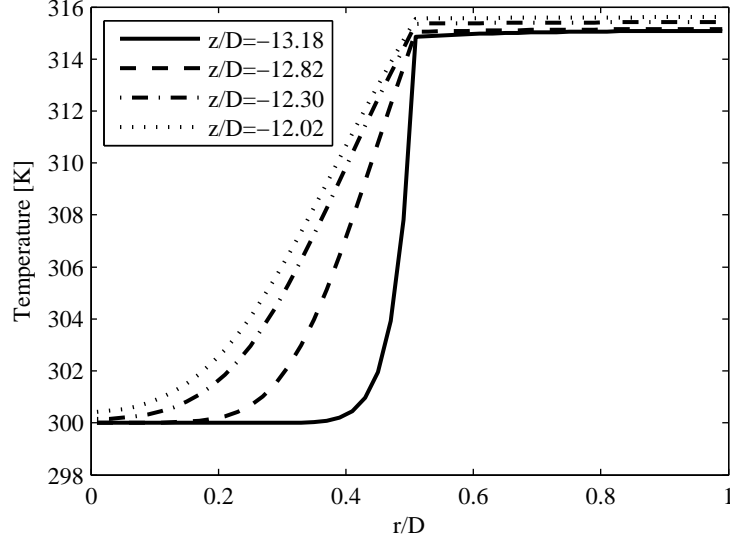


Figure 3-4: The temperature profile in the radial direction for the case of $\phi = 0.75$, $\bar{u}_{in} = 1.3$ m/s, $\kappa = 2R = 1$ mm, $\lambda_{fh} = 10$ W/mK, at different values of z/D .

W/mK, the drop in the heat flux near the bottom surface is not drastic. In this case, the temperature of the bottom surface of the plate is higher than the ambient temperature, $T_{bot} \simeq 316$ K. The convective heat loss rate from the bottom surface when $\lambda_{fh} = 10$ W/mK is $\dot{q}_{loss} \simeq hA_{bot}(T_{bot} - T_o) = 0.19$ mW, where h is the heat transfer coefficient at the bottom surface, which is assumed as 5 W/m²K in this study, A_{bot} is the plate surface area, and T_o is the ambient temperature, assumed to be 300 K. Note that the heat loss rate is negligible compared to the total heat generation by the flame, 2.4 W; thus the total energy is almost conserved, and the thermal energy is recycled between the flame and the fresh reactants through the plate.

For both the conductive plate cases, results in Fig. 3-3 show that the heat flux at the bottom surface undergoes a sudden jump. This is a result of the thermal entrance boundary condition: the temperature profile of the gas at the upstream end of the computational domain is assumed to be a uniform profile. This, however, does not impact the results significantly. In order to illustrate this, in Fig. 3-4 I plot the temperature profile along the radial direction at different streamwise locations when $\lambda_{fh} = 10$ W/mK. While the uniform temperature profile is imposed at $z/D = -13.20$, at $z/D > -12.30$ the temperature profile is fully developed and the heat

flux from the gas is well behaved from there on (Fig. 3-3). Thus, the flow loses memory of this entrance effect within a maximum of 10 grid points, as the thermal boundary layer develops. To further confirm this weak impact of the inlet thermal boundary condition, I ran cases which imposed a Neumann boundary condition on the temperature at the bottom side of the domain and obtained identical results. This could have been expected, given the very large aspect ratio of the holes in the perforated plate, $L/D = 13.20$, which is common in practical applications. The heat loss from the bottom side of the plate is extremely weak and nearly all the thermal energy lost to the top side of the plate is recycled to the gas through the side walls of the hole. For large L/D ratios and low velocities, as in the current setup, the assumption that the inlet velocity is fully developed is justified. For the range of parameters used, a weak dependence of the solution on the inflow boundary conditions is observed. The development of the thermal and momentum boundary layers lead to a fully developed temperature and velocity profiles. A more elaborate approach for the treatment of the inflow boundary conditions is essential when a small aspect ratio plate and high convective cooling at the bottom surface is of interest.

Figure 3-5 shows the fuel mass fraction contours for the same cases shown in Fig. 3-1. The shape of the fuel mass fraction contours are very similar to the shape of the temperature contours, when $\lambda_{fh} = 0$, as expected for an adiabatic flame with near unity Lewis number. In the flame zone, the fuel mass diffusion layer thickness is smaller than the thermal diffusion layer thickness. The thicker thermal diffusion layer is mainly generated as a result of the slow CO oxidation reaction. When the gas-plate heat exchange is allowed, the shape of the fuel mass fraction contours are significantly different than the shape of the temperature contours; the presence of heat exchange between the gas and the plate (but no mass transfer) creates significant mismatch between the temperature and species profiles.

Next, the contours of the volumetric heat-release rate and the velocity vectors are shown in Fig. 3-6. The burning rate near the flame tip drops slightly and the flame tends to spread out when gas-plate heat exchange is allowed, or the flame becomes weaker. There is a stagnation region around the flame base. In all the cases, the

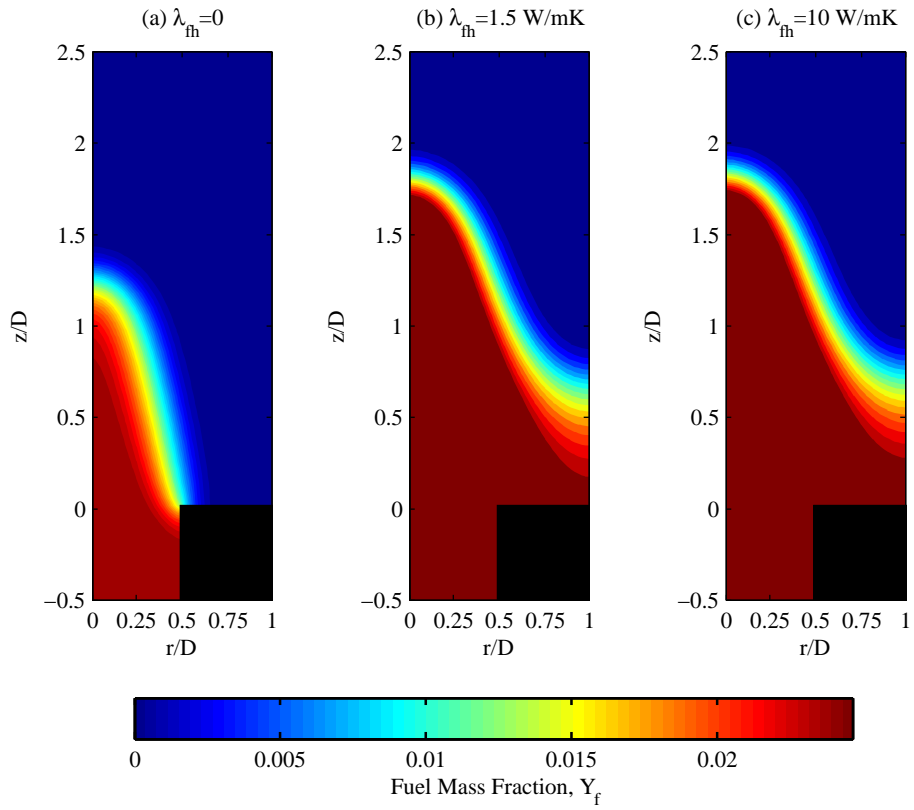


Figure 3-5: The fuel mass fraction contours for the case of $\phi = 0.75$, $\bar{u}_{in} = 1.3$ m/s, $\kappa = 2R = 1$ mm, and (a) $\lambda_{fh} = 0$, (b) $\lambda_{fh} = 1.5$ W/mK, and (c) $\lambda_{fh} = 10$ W/mK.

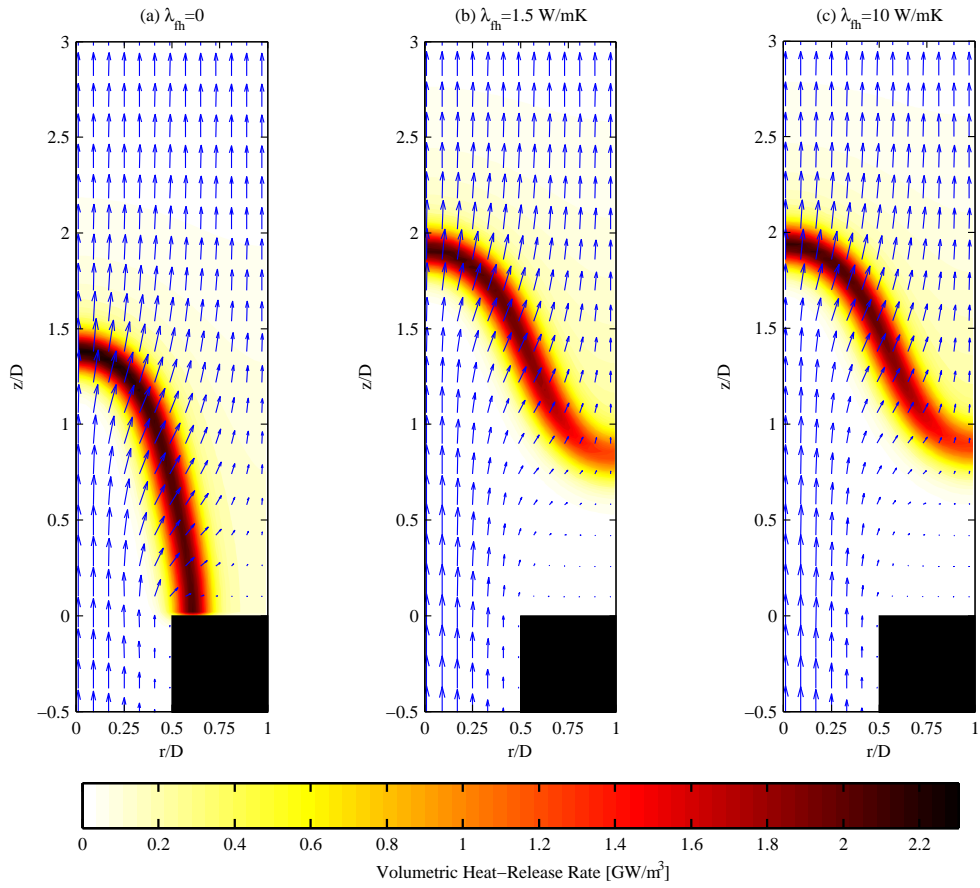


Figure 3-6: Volumetric heat release rate contours and velocity vectors for the case of $\phi = 0.75$, $\bar{u}_{in} = 1.3 \text{ m/s}$, $\kappa = 2R = 1 \text{ mm}$, with (a) $\lambda_{fh} = 0$, (b) $\lambda_{fh} = 1.5 \text{ W/mK}$, and (c) $\lambda_{fh} = 10 \text{ W/mK}$.

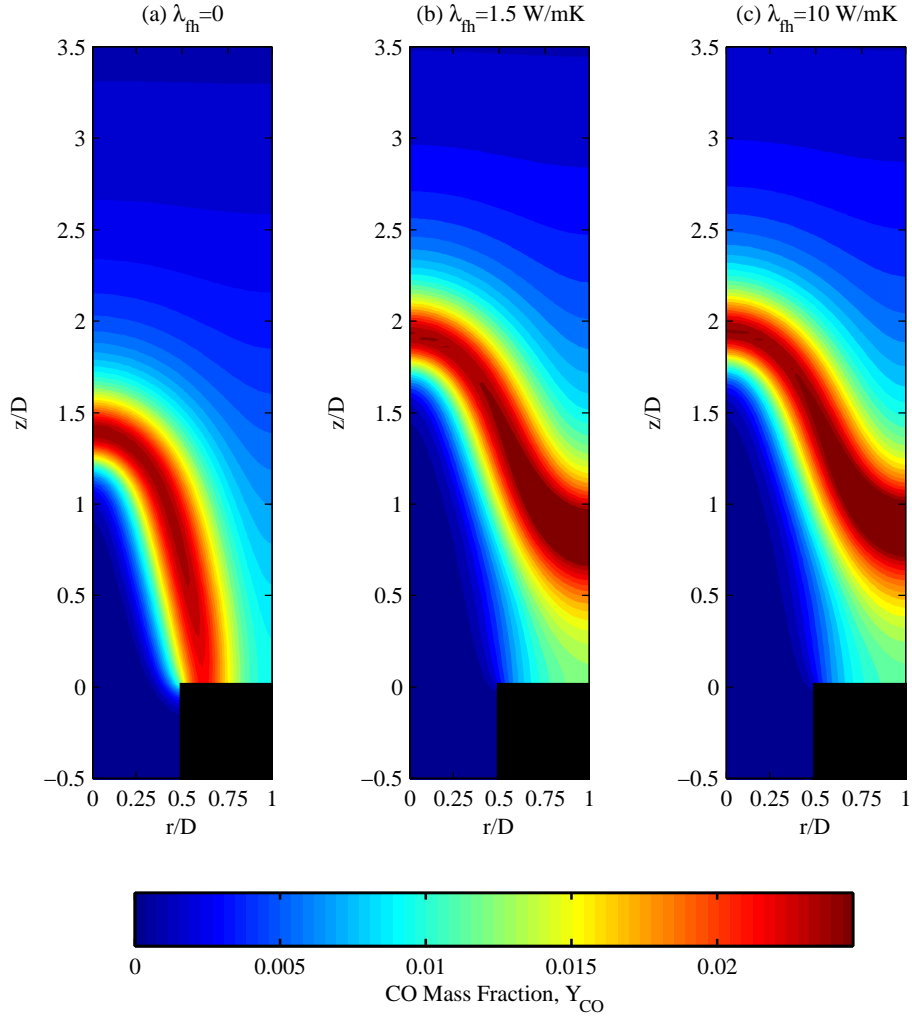


Figure 3-7: The CO mass fraction contours for the case of $\phi = 0.75$, $\bar{u}_{in} = 1.3$ m/s, $\kappa = 2R = 1$ mm, and (a) $\lambda_{fh} = 0$, (b) $\lambda_{fh} = 1.5$ W/mK, and (c) $\lambda_{fh} = 10$ W/mK.

volumetric heat-release rate is finite near the flame base (see the thick light yellow bands in Fig. 3-6). In order to investigate this, in Fig. 3-7, I plot the CO mass fraction contours, one of the primary intermediate species. The CO mass fraction reaches its maximum near the flame base. The diffusion thickness of CO is larger near the flame base region than the flame tip region. Complex interactions take place around the flame base region and an in-depth physical analysis of this stagnation zone is warranted in future studies.

In Fig. 3-8, the streamwise velocity obtained from non-reactive and reactive simulations at different values of λ_{fh} along the z direction starting from the top surface of

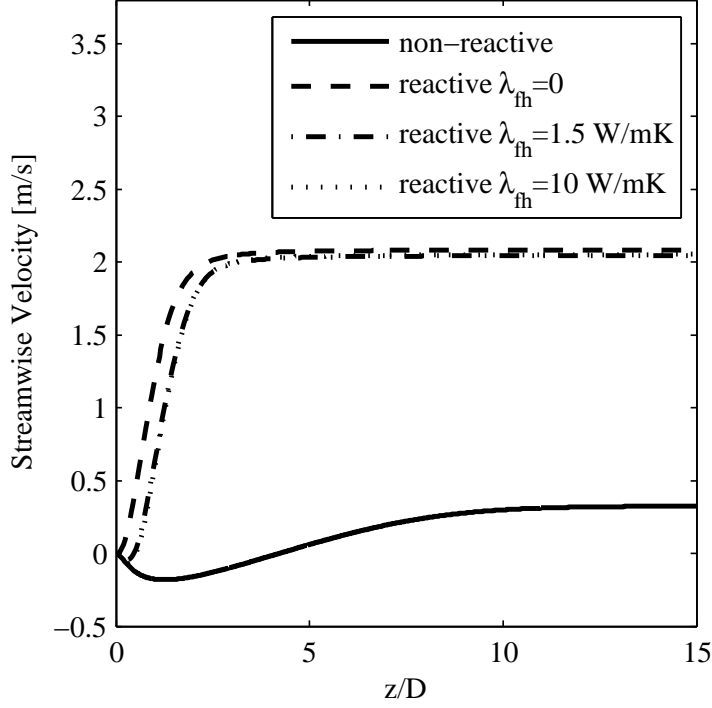


Figure 3-8: The streamwise velocities along the z direction at $r/D = 0.99$ computed under non-reactive and reactive conditions with different values of λ_{fh} , $\bar{u}_{in} = 1.3$ m/s, $\kappa = 2R = 1$ mm, $\phi = 0.75$.

the plate at $r/D = 0.99$ is plotted. The figure clearly shows that under non-reactive conditions there is a recirculation zone extending in the range $0 < z/D < 4.3$. The formation of the recirculation zone is prevented by the flame when $\lambda_{fh} = 0$. A very narrow recirculation zone forms when $\lambda_{fh} = 1.5$ W/mK and $\lambda_{fh} = 10$ W/mK, extending in the range $0 < z/D < 0.5$. Because of the flame stand-off distance, the temperature downstream of the plate is lower compared to the case with $\lambda_{fh} = 0$, which allows a narrow recirculation zone to form.

Next, for all the three cases, the consumption speed of the flame at the centerline, $S_{c,0}$, and along the z direction at $r/D = 1$ ($r = \kappa$), $S_{c,\kappa}$, using Eq. (2.9), is computed. The consumption speeds are summarized in Table 3.1. The laminar burning velocities of planar unstretched flame at $\phi = 0.75$, obtained using the 1-D code developed in our group (see Fig. 2-8), is $S_L = 20.9$ cm/s.

The consumption speed of the flame at the centerline for the case of $\lambda_{fh} = 0$ is

| | $\lambda_{fh} = 0$ | $\lambda_{fh} = 1.5 \text{ W/mK}$ | $\lambda_{fh} = 10 \text{ W/mK}$ |
|-----------------------|--------------------|-----------------------------------|----------------------------------|
| $S_{c,0}$ [cm/s] | 22.3 | 21.3 | 21.4 |
| $S_{c,\kappa}$ [cm/s] | – | 22.3 | 22.5 |

Table 3.1: The flame consumption speeds along the centerline, $S_{c,0}$, and along the z direction at $r/D=1$, $S_{c,\kappa}$ at different values of λ_{fh} , $\phi = 0.75$ m/s, $\kappa = 2R = 1$ mm, $\bar{u}_{in} = 1.3$ m/s. The laminar burning velocity of a planar unstretched flame at $\phi = 0.75$ is $S_L = 20.9$ cm/s.

higher compared to the laminar burning velocity of a corresponding planar flame. It is known that a negative curvature (flame concave towards the reactants) acts to increase the flame burning velocity [5, 15], when the radius of curvature of the flame is comparable with the flame thickness. The values of $S_{c,0}$ are slightly lower when heat exchange is allowed compared to the case with $\lambda_{fh} = 0$, primarily because the flame becomes weaker as discussed before. With heat exchange, the flame is thick along the z direction at $r/D = 1$, i.e. along the flame base. Figure 3-6 shows that the volumetric heat release rate downstream of the flame base is finite for a thicker region. These effects results in $S_{c,\kappa} > S_{c,0}$. These phenomena are related to the physics in the stagnation region near the positively curved flame base.

3.2 Effect of the equivalence ratio

Simulations at $\phi = 0.85$, $\phi = 0.75$, and $\phi = 0.65$ were performed. The other parameters were kept constant at: $\bar{u}_{in} = 1.3$ m/s, $\kappa = 2R$, and $\lambda_{fh} = 1.5$ W/mK. The corresponding Zeldovich numbers are $Ze_{0.85} = 10.06$, $Ze_{0.75} = 10.7$, $Ze_{0.65} = 11.5$ (assuming $\frac{E_a}{R} = 24400$ K). The inlet Reynolds number based on the maximum velocity is $Re = 162$ and the plate thickness ratio is $(t/D_p) = 13.2$. At $\phi = 0.65$, the flame blows out (moves out of the domain without stabilizing), as a result of the heat loss; although when the plate was adiabatic ($\lambda_{fh} = 0$), the flame could be stabilized.

In Fig.3-9, the temperature contours at $\phi = 0.85$, and $\phi = 0.75$ are shown. As expected, the flame cools down as ϕ decreases. The laminar flame speed decreases as ϕ decreases (see Fig. 2-8). This results in larger flame cone angle, so as to further reduce the flow velocities normal to the flame. At all equivalence ratios, the temperature

contours become horizontal downstream of the plate surfaces as a result of the heat loss. The flame stand-off distance decreases along the radial direction and it increases as ϕ decreases.

Figure 3-10 shows the heat flux from the gas to the top surface of the perforated-plate as a function of the radial coordinate at both equivalence ratios. The heat flux increases along the radial direction, and also with the equivalence ratio, due to decreasing flame stand-off distance. Fig. 3-10 shows the top surface temperature of the perforated-plate, T_s , as a function of the radial coordinate. As ϕ increases, T_s increases as a result of higher heat transfer rate. The heat flux from the perforated-plate side surface to the gas as a function of the streamwise coordinate at both equivalence ratios is shown in Fig. 3-11. The heat flux is the largest close to the top surface, and close to zero at the bottom surface at both equivalence ratios. This suggests that all the heat transferred from the gas to the plate from the top surface is transferred back to the gas from the side surface, conserving the total enthalpy.

Figure 3-12 shows the contours of the volumetric heat release rate and the velocity vectors. The maximum value of the volumetric heat release rate decreases as ϕ decreases. Because of the mismatch between the temperature and species profiles due to heat transfer to the plate, the maximum value of the volumetric heat release rate downstream of the plate is smaller than that at the centerline especially at high ϕ (more heat transfer). At both values of ϕ , the volumetric heat release rate along the z direction at $r/D = 1$ is finite downstream of the location where the volumetric heat release rate is at its maximum value. This effect becomes more significant as ϕ drops since the flame moves closer to the right domain boundary, which is the boundary of the adjacent flame. This effect causes the total burning rate along the z direction at $r/D = 1$ to exceed that at the centerline. This is shown in table 3.2, where consumption speeds along the centerline and along the z direction at $r/D = 1$ are reported. These observations show that at an equivalence ratio in the range $0.75 < \phi < 0.85$, $S_{c,\kappa} = S_{c,0}$, similar to the assumption of the theoretical model developed in Ref [1].

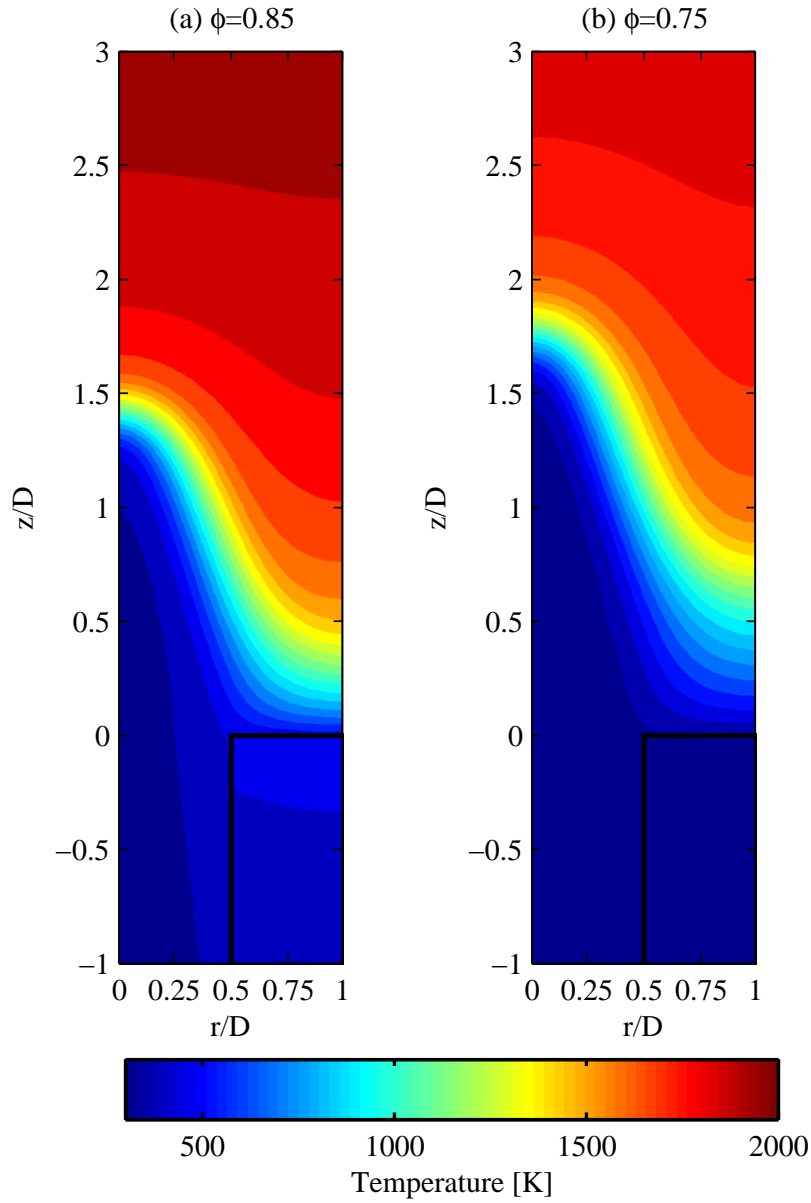


Figure 3-9: The temperature contours of steady flames for the case of a conductive perforated-plate, $\lambda_{fh} = 1.5$ W/mK, $\bar{u}_{in} = 1.3$ m/s, $\kappa = 2R = 1$ mm, at (a) $\phi = 0.85$, and (b) $\phi = 0.75$.

| | $\phi = 0.85$ | $\phi = 0.75$ | $\phi = 0.65$ |
|-----------------------|---------------|---------------|---------------|
| $S_{c,0}$ [cm/s] | 27.0 | 21.3 | BLOWOUT |
| $S_{c,\kappa}$ [cm/s] | 19.7 | 22.3 | BLOWOUT |

Table 3.2: The flame consumption speeds along the centerline and along the z direction at $r/D=1$ for the case of a conductive perforated-plate, $\lambda_{fh} = 1.5$ W/mK, $\bar{u}_{in} = 1.3$ m/s, $\kappa = 2R = 1$ mm, at different values of ϕ .

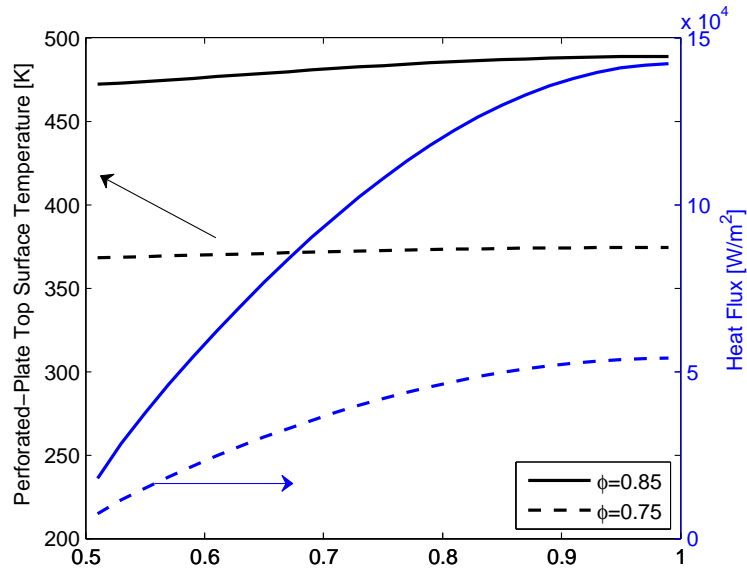


Figure 3-10: The heat flux from the gas to the perforated-plate top surface and the perforated-plate top surface temperature; as a function of r/D at $\phi = 0.85$, and $\phi = 0.75$. $\lambda_{fh} = 1.5 \text{ W/mK}$, $\bar{u}_{in} = 1.3 \text{ m/s}$, $\kappa = 2R = 1 \text{ mm}$

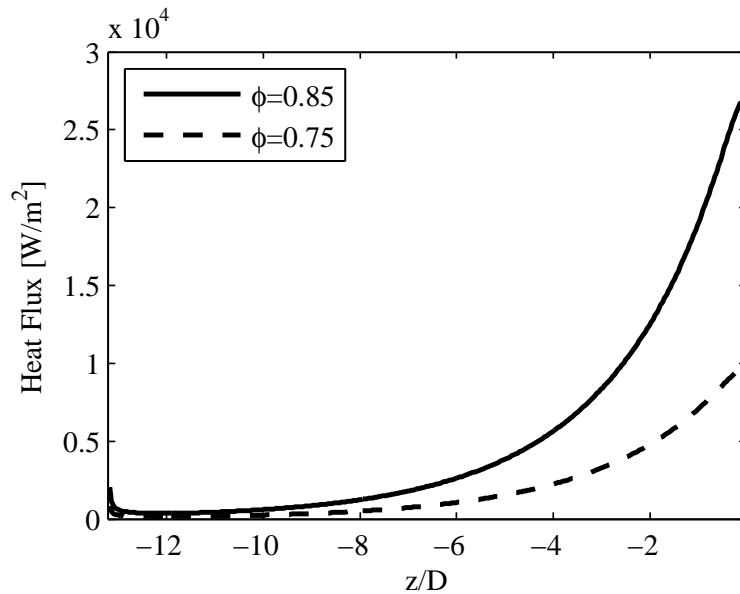


Figure 3-11: The heat flux from the perforated-plate side surface to the gas as a function of z/D at $\phi = 0.85$, and $\phi = 0.75$. $\lambda_{fh} = 1.5 \text{ W/mK}$, $\bar{u}_{in} = 1.3 \text{ m/s}$, $\kappa = 2R = 1 \text{ mm}$

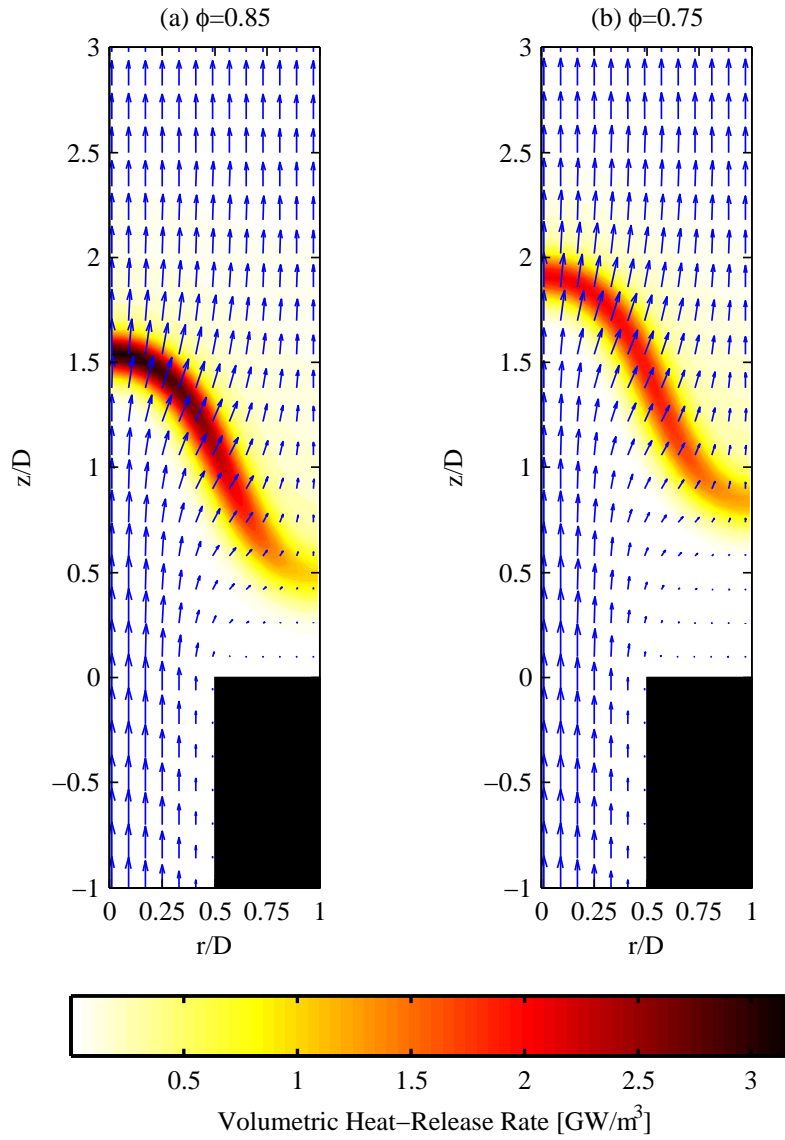


Figure 3-12: The contours of the volumetric heat release rate and the velocity vectors for the case of a conductive perforated-plate, $\lambda_{fh} = 1.5 \text{ W/mK}$, $\bar{u}_{in} = 1.3 \text{ m/s}$, $\kappa = 2R = 1 \text{ mm}$, at (a) $\phi = 0.85$, and (b) $\phi = 0.75$.

3.3 Effect of the mean inlet velocity

Now, the impact of the mean inlet velocity on the steady flame characteristics are investigated. Simulations at $\bar{u}_{in} = 0.8$ m/s and $\bar{u}_{in} = 1.3$ m/s are performed, while keeping the other parameters constant at $\phi = 0.75$, $\kappa = 2R$, and $\lambda_{fh} = 1.5$ W/mK. The corresponding inlet Reynolds number based on the maximum velocity are $Re = 100$ and $Re = 162$ respectively. The Zeldovich number is $Ze = 10.7$ and the plate thickness ratio is $(t/D_p) = 13.2$.

Figure 3-13 shows the contours of the volumetric heat release rate and the velocity vectors at both values of the inlet velocity. As expected, the entire flame surface moves downstream and the flame angle increases when the inlet velocity increases. Because the positively curved region stabilizes further downstream from the plate at higher inlet velocity, the top surface temperature of the plate is lower as shown in Fig. 3-14, resulting in smaller heat transfer rate between the gas and the plate. The burning rate at the centerline increases as the inlet velocity increases, primarily due to the effect of higher flame tip curvature.

In Table 3.3, the consumption speeds calculated at the centerline and along the z direction at $r/D=1$ are reported. As noted in the previous consumption speeds descriptions, the thickness of the flame (or the region of finite volumetric heat release rate) and the peak volumetric heat release rate impact the consumption speeds, as it is an integral quantity (see Eq. 2.9). For the case with higher mean inlet velocity ($\bar{u}_{in} = 1.3$ m/s.), although the peak volumetric heat release rate is higher along the centerline as compared to the edge of the domain (see Fig. 3-14), the region with finite volumetric heat release rate is thicker along the edge. This results in $S_{c,\kappa} > S_{c,0}$. However, this is not observed when the mean inlet velocity is, $\bar{u}_{in} = 0.8$ m/s. For this case, the heat transfer rate to the plate is higher as compared to the higher velocity case as the flame is closer to the plate. This results in the flame base for the lower velocity case to be weaker compared to the flame base of the higher velocity case. As seen with the equivalence ratio parameter, at a mean inlet velocity in the range $0.8 < \bar{u}_{in} < 1.3$ [m/s], $S_{c,\kappa} = S_{c,0}$.

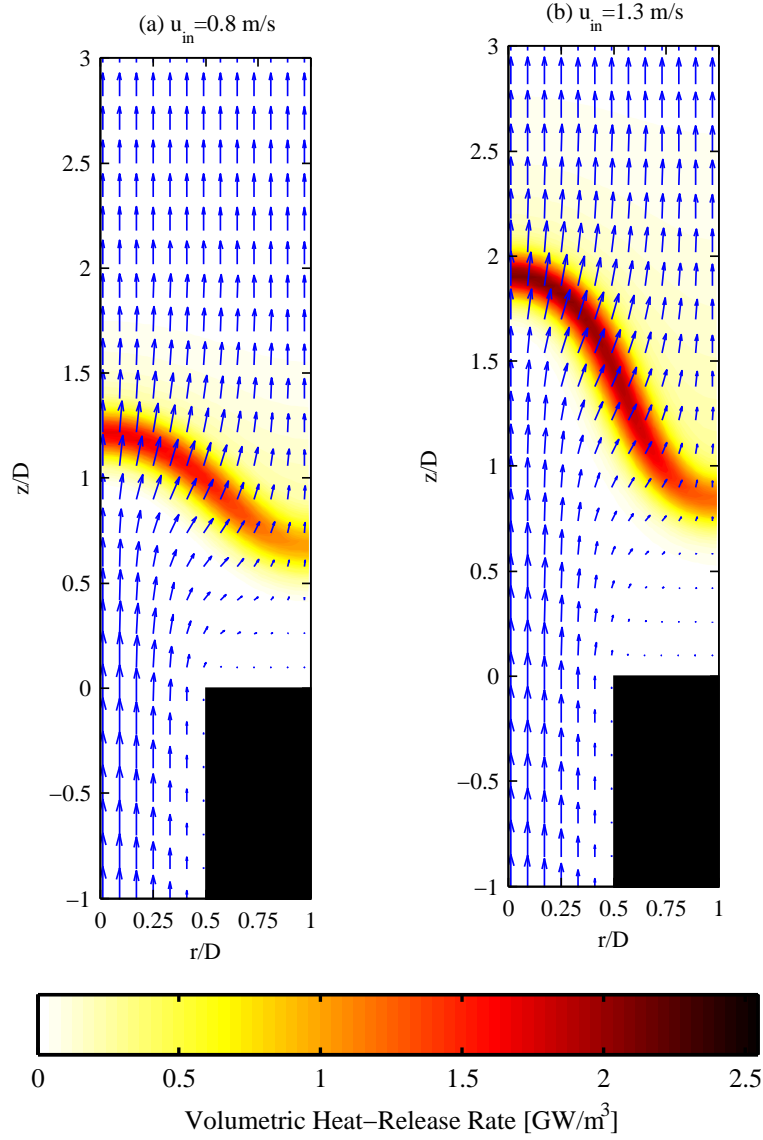


Figure 3-13: The contours of the volumetric heat release rate and the velocity vectors for the case of a conductive perforated-plate, $\lambda_{fh} = 1.5$ W/mK, $\phi = 0.75$, $\kappa = 2R = 1$ mm, (a) $\bar{u}_{in} = 0.8$ m/s, and (b) $\bar{u}_{in} = 1.3$ m/s.

| | $\bar{u}_{in} = 0.8$ m/s | $\bar{u}_{in} = 1.3$ m/s |
|-----------------------|--------------------------|--------------------------|
| $S_{c,0}$ [cm/s] | 17.4 | 21.3 |
| $S_{c,\kappa}$ [cm/s] | 16.0 | 22.3 |

Table 3.3: The flame consumption speeds along the centerline and along the z direction at $r/D=1$ for the case of a conductive perforated-plate, $\lambda_{fh} = 1.5$ W/mK, $\phi = 0.75$ m/s, $\kappa = 2R = 1$ mm, at different values of \bar{u}_{in} .

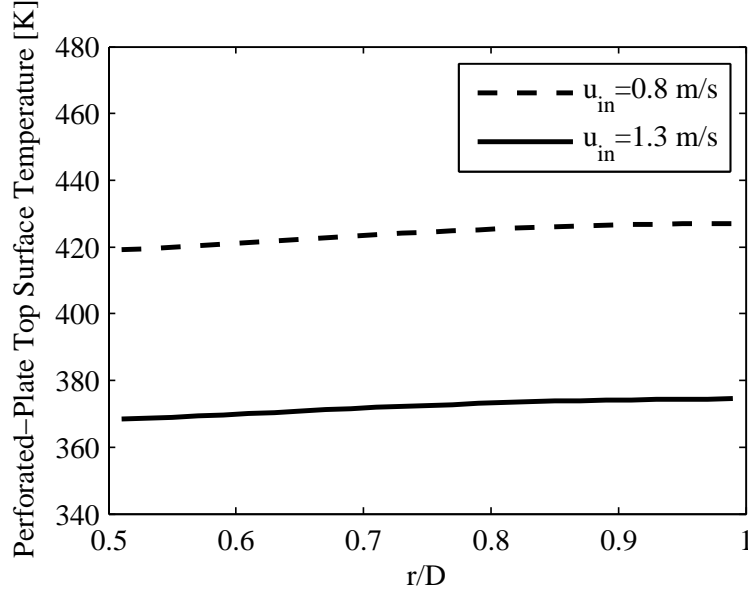


Figure 3-14: The perforated-plate top surface temperatures as a function of r/D for the case of a conductive perforated-plate, $\lambda_{fh} = 1.5$ W/mK, $\phi = 0.75$ m/s, $\kappa = 2R = 1$ mm, at different values of \bar{u}_{in} .

3.4 Effect of distance between two adjacent holes

Next, the impact of the distance between adjacent holes on the steady flame characteristics is investigated. Simulations with $\kappa = 2R = 1$ mm and $\kappa = 3R = 1.5$ mm are performed, while keeping the other parameters constant at $\phi = 0.75$, $\bar{u}_{in} = 1.3$ m/s, and $\lambda_{fh} = 1.5$ W/mK. The corresponding plate thickness ratios are $(t/D_p)_{2R} = 13.2$ and $(t/D_p)_{3R} = 6.6$. The inlet Reynolds number based on the maximum velocity is $Re = 162$ and Zeldovich number is $Ze = 10.7$.

Figure 3-15 shows the contours of the volumetric heat-release rate and the velocity vectors at both values of κ . The burning rate downstream of the plate surface significantly drops when κ is increased. Because the total plate surface area increases, resulting in higher overall heat transfer rate from the gas to the plate, the mismatch between the temperature and the species profiles is more significant. As a result of the higher heat transfer from the gas to the plate, (i) as shown in Fig. 3-16, the plate surface temperature is significantly higher when $\kappa = 3R$; (ii) as shown in Fig. 3-17, where the temperature profiles along the centerline for both cases are compared, the reactant mixture is preheated more before entering the reaction zone, and (iii) the

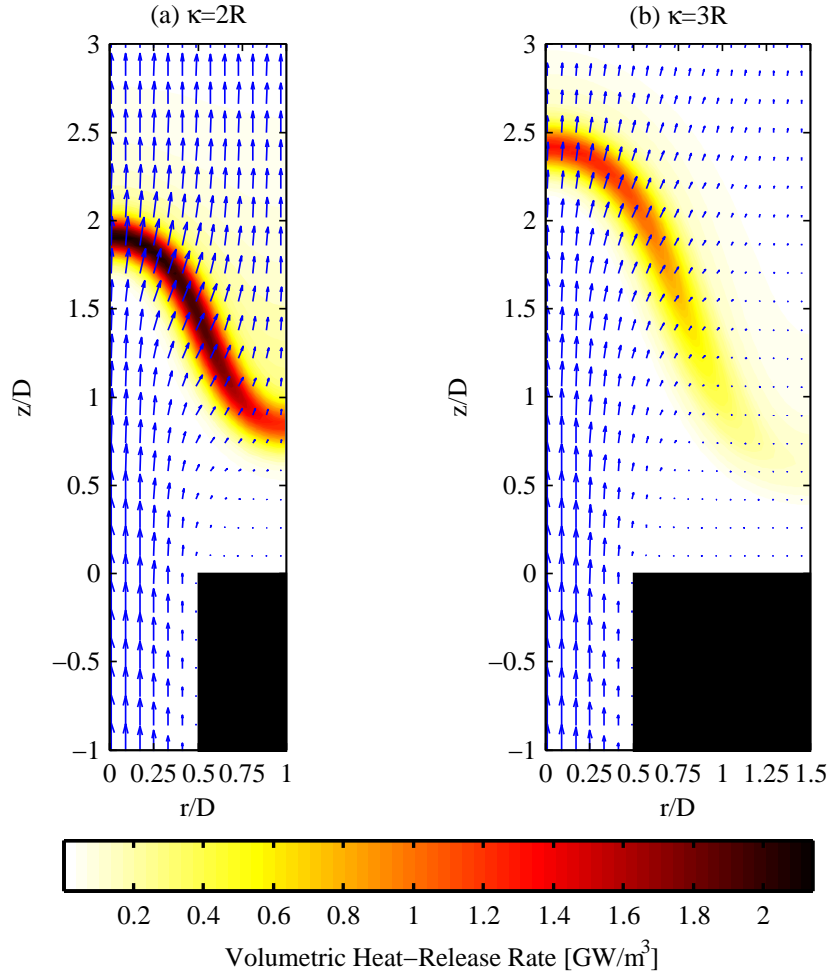


Figure 3-15: The contours of the volumetric heat release rate and the velocity vectors for the case of a conductive perforated-plate, $\lambda_{fh} = 1.5 \text{ W/mK}$, $\phi = 0.75$, $\bar{u}_{in} = 1.3 \text{ m/s}$, (a) $\kappa = 2R$, and (b) $\kappa = 3R$.

flame stand-off distance decreases. The heat loss effects are dominant compared to the preheating effects as mentioned before, the burning rate at the centerline decrease when κ increases.

All these observations are summarized in Table 3.4, where the consumption speeds along the centerline, along the z direction at the right domain boundary ($r/D=1$ when $\kappa = 2R$, $r/D=1.5$ when $\kappa = 3R$) are reported.

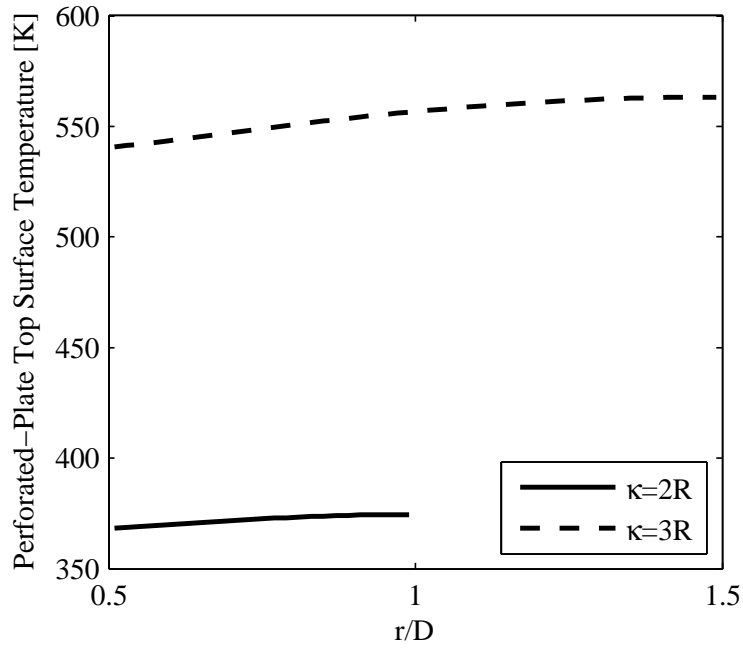


Figure 3-16: The perforated-plate top surface temperatures as a function of r/D for the case of a conductive perforated-plate, $\lambda_{fh} = 1.5 \text{ W/mK}$, $\phi = 0.75 \text{ m/s}$, $\bar{u}_{in} = 1.3 \text{ m/s}$, at different values of κ .

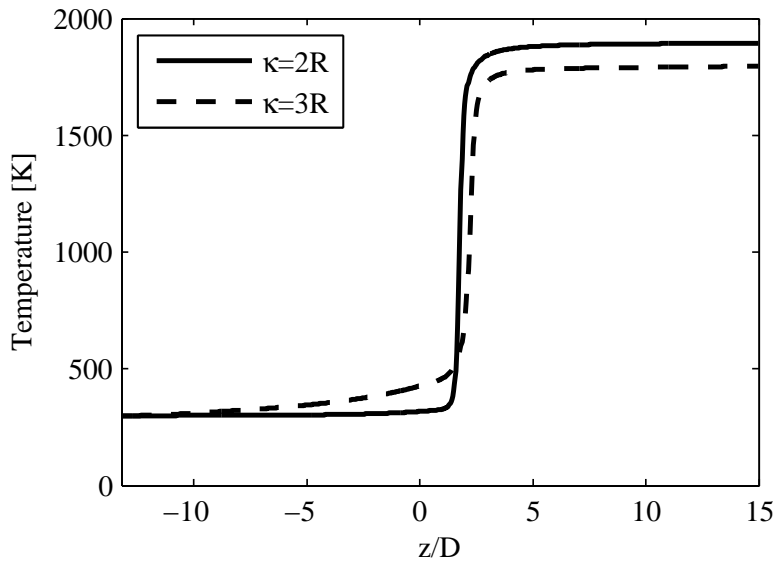


Figure 3-17: The temperature profiles along the centerline for the case of a conductive perforated-plate, $\lambda_{fh} = 1.5 \text{ W/mK}$, $\phi = 0.75 \text{ m/s}$, $\bar{u}_{in} = 1.3 \text{ m/s}$, at different values of κ .

| | $\kappa = 2R$ | $\kappa = 3R$ |
|-----------------------|---------------|---------------|
| $S_{c,0}$ [cm/s] | 21.3 | 14.5 |
| $S_{c,\kappa}$ [cm/s] | 22.3 | 6.1 |

Table 3.4: The flame consumption speeds along the centerline and along the z direction at $r/D=1.5$ for the case of a conductive perforated-plate, $\lambda_{fh} = 1.5$ W/mK, $\phi = 0.75$ m/s, $\bar{u}_{in} = 1.3$ m/s, at different values of κ .

3.5 Single-Step Chemical Kinetics

A single-step kinetic mechanism reproduces the flame response qualitatively reasonably well, for burner configurations similar to the one analyzed in this thesis. However, quantitative details may be different. Comparison of simulations using a single-step mechanism proposed by [46] (Table II, set 3, pp 36) with the multi-step UCSD reduced mechanism, was performed. It was observed that the flame consumption speed along the centerline was significantly different compared to the detailed kinetic mechanism, for an adiabatic plate. This is expected because the data in the rate equations were obtained to match experimentally observed flame speeds and flammability limits under certain conditions. The flame structure computed using the single-step kinetics was also different. Figure 3-18 shows a comparison between simulation with a single-step kinetics and detailed kinetics, for the case of an adiabatic perforated plate, $\phi = 0.75$ and $\bar{u}_{in} = 0.8$ m/s. The centerline consumption speed, $S_{c,0} = 12.1$ cm/s for the single-step mechanism case as compared to $S_{c,0} = 19.7$ cm/s for the UCSD reduced mechanism. The flame location, curvature and the gradients in the temperature contours are qualitatively similar but differ quantitatively. Further more, the single-step chemistry is unable to capture the gradual decrease in the heat release rate in the products (see the centerline heat release rate plot), which is a feature of multi-step kinetic mechanisms.

Moreover, using the same set of parameters, the flame could not be stabilized using the single-step mechanism, within the range of parameters explored in this chapter, in the presence of heat exchange with the plate. The single-step mechanism parameters needs to be adjusted to stabilize flames under such conditions, as noted by de Goey et. al. [9]. A unique single-step mechanism for a system with varying

parameters may not be entirely satisfactory for numerical analysis.

3.6 Conclusions

In this chapter, two-dimensional simulations of steady, laminar, perforated-plate stabilized methane-air flames using a reduced chemical kinetics mechanism are performed. I solved for the temperature profile within the perforated-plate by allowing for heat exchange between the gas mixture and the solid plate. I varied the thermal conductivity of the plate, the equivalence ratio, the mean inlet velocity, and the distance between adjacent holes to investigate the impact of the operating conditions, the thermal properties and the design of the plate on the steady flame characteristics.

The results show that when the gas-plate heat exchange is neglected, that is, assuming an adiabatic plate, a conical flame forms downstream of the holes, which is anchored near the edge of the plate. When the gas-plate heat exchange is allowed, a positively curved flame forms downstream of the plate surface, connecting the adjacent conical flames. The curvature of this flame is larger for closer holes. For certain operating conditions, it is possible to have a flame stabilized in the presence of an adiabatic plate, which may blowout if flame-wall interactions are allowed.

When the thermal conductivity of the plate increases, the temperature of the plate surface exposed to the ambient rises, causing the thermal entrance effects to be significant at the hole inlet. The heat flux from the gases to the plate decreases with increasing thermal conductivity, which reduces the plate's surface temperature.

As the equivalence ratio increases, the heat transfer to the plate increases, the flame cone angle decreases, the positively curved flame moves closer to the perforated-plate, which increases the plate's surface temperature. The consumption speed of the flame tip is lower compared to the adiabatic flames. As the equivalence ratio decreases, the consumption speed of the flame tip decreases, while the consumption speed of the positively curved flame downstream of the plate increases. At a particular value of the equivalence ratio, the consumption speed along the flame surface becomes uniform.

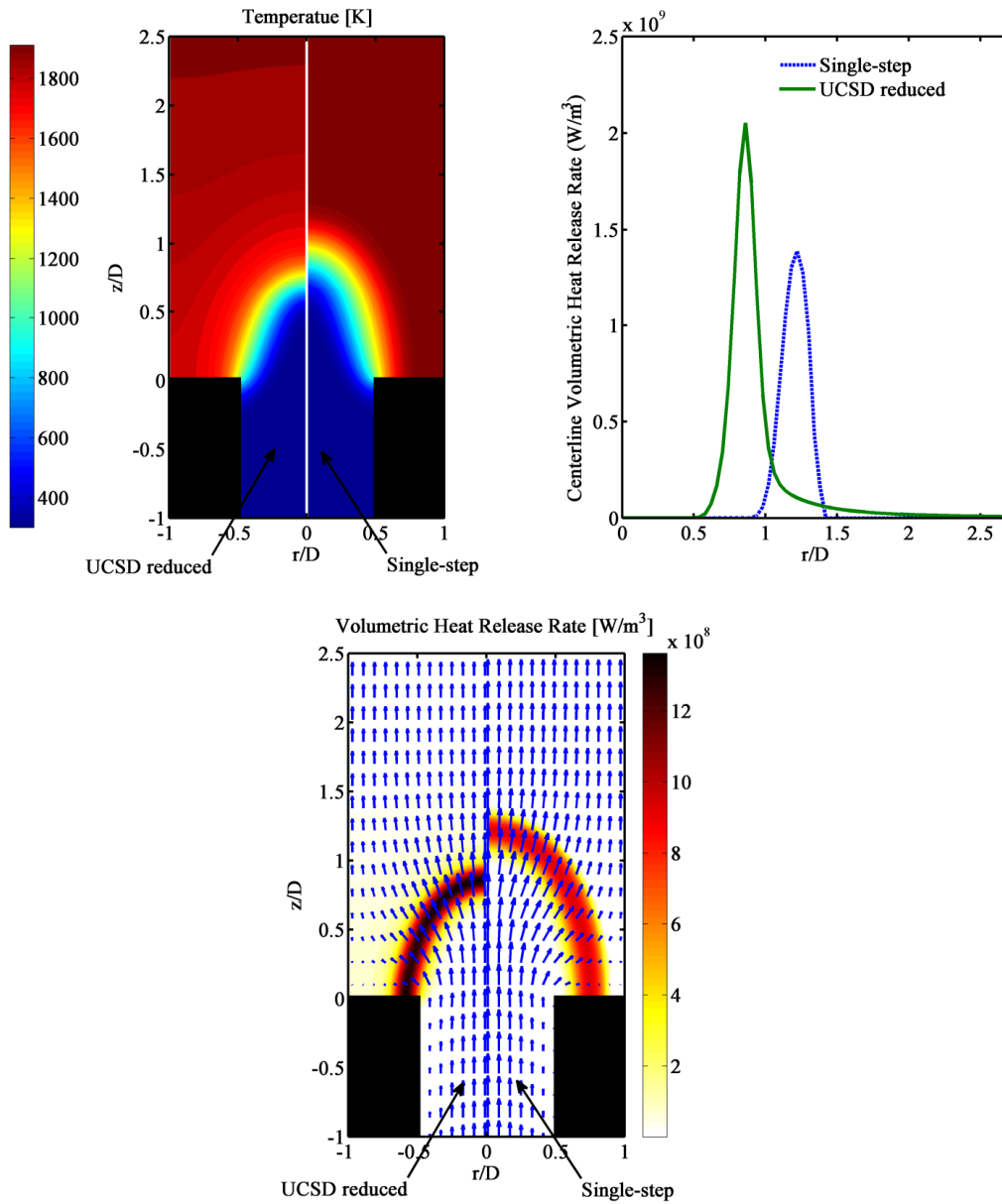


Figure 3-18: Comparison of single-step and multi-step (UCSD reduced) kinetic mechanism simulations, for the case of an adiabatic perforated-plate, $\phi = 0.75$, $\bar{u}_{in} = 0.8$ m/s

| | Increasing λ_{fh} | Increasing ϕ | Increasing \bar{u}_{in} | Increasing κ |
|----------------|---------------------------|-------------------|---------------------------|---------------------|
| H | Increases | Decreases | Increases | Increases |
| ψ_f | Increases | Decreases | Increases | Increases |
| T_s | Decreases | Increases | Decreases | Increases |
| $S_{c,0}$ | Increases | Increases | Increases | Decreases |
| $S_{c,\kappa}$ | Increases | Decreases | Increases | Decreases |

Table 3.5: Summary of the parametric study of steady, laminar perforated-plate stabilized flames in the presence of gas-plate heat exchange.

As the mean inlet velocity rises, the flame stabilizes further away from the plate's top surface, the steepness of the flame increases, the heat flux to the plate decreases, which decreases the plate's surface temperature. Because the flame tip curvature increases when the flame stabilizes further downstream, the consumption speed of the flame tip is higher.

When the distance between the holes is small, and as the equivalence ratio drops, a convex flame forms close to the plate. The consumption speed of this positively curved flame exceed that of the negatively curved flame tip. As the distance between the holes increases, the total heat transfer rate to the plate increases and the consumption speed of the part of the flame between the holes drops. Because of the higher heat transfer to the plate, the top surface temperature of the plate rises, reducing the flame stand-off distance.

These results show the strong dependence of the flame characteristics on the perforated-plate design and thermal properties. The major results of this parametric study are summarized in Table 3.5, where the impacts of λ_{fh} , ϕ , \bar{u}_{in} , and κ on the distance between the plate surface and the flame tip, H ; the flame stand-off distance, ψ_f ; the top surface temperature of the plate, T_s ; the consumption speed at the centerline, $S_{c,0}$; and the consumption speed calculated along the z direction at the right domain boundary, $S_{c,\kappa}$ are reported.

Chapter 4

Flame Dynamics

The analysis in this chapter is divided into two parts. I first discuss the linear transfer function of the flame response to small inlet velocity perturbations. The linear transfer function is defined as

$$\text{TF}(f) = \frac{Q'/Q}{u'/u} \quad (4.1)$$

where f is the frequency of the velocity perturbation. I then discuss the nonlinear response of the flame to finite amplitude inlet velocity oscillations and the impact of different physical processes on the flame response, in the time domain. The following parameters are kept constant throughout the simulations: $R = 0.5$ mm; $L = 13.2$ mm; $L_d = 15$ mm; $T_{in} = 300$ K; $\text{Pr} = 0.71$; $\rho_{fh} = 2400$ kg/m³; $c_{fh} = 1070$ J/kgK. I perform parametric studies by varying the following: ϕ ; \bar{u}_{in} , λ_{fh} , and κ .

4.1 Linear Transfer Functions

The steady-state solution for a given set of operating parameters is used as the initial solution. The flame response to a 10% step increase in the inlet velocity is computed. The total heat release rate and other response parameters are sampled between the time when the step change is applied and when the new steady state is reached. The transfer function can be equivalent to the Fourier transform of the response to a unit impulse of velocity, i.e. the simulated step response is transformed into an impulse

response. This is shown in the form of Bode plots in Fig. 4-1. To ensure that a 10% jump is within the linear range, smaller jumps were introduced and the insensitivity of the amplitude of the impulse was verified. Similar amplitudes for the velocity impulse were used in [9]. The gain in the Bode plots is non-dimensionalized with respect to the mean values of the heat release rate.

Figure 4-1 shows the impact of the heat exchange with the burner surface and the kinetics mechanism on the response of the total heat release rate, Q_f , to inlet velocity perturbation, for cases with $\phi = 0.75$, $\bar{u}_{in} = 0.8$ m/s, and $\kappa = 2R = 1$ mm. Q_f is obtained by integrating the volumetric heat release rate throughout the cylindrical domain. The case with the adiabatic wall was computed using a single-step and a multi-step mechanism. The case with heat exchange with the wall was computed with the detailed mechanism. Single-step mechanism, same as used in chapter 3, predicts the low frequency behavior reasonable well. I did not use any numerical post processing in the Bode plots for the case with multi-step mechanism; however I had to use smoothening for the single-step results. Nevertheless, for the single-step results, there are spurious oscillations at higher frequencies, making the results quantitatively unreliable at such frequencies. At higher frequencies, the time scales of the consumption of different species are comparable to the flow time scales. A detailed kinetics mechanism is able to capture the impact of the flow oscillations on the evolution of individual species consumption and production rates, resulting in smooth curves in the Bode plot. This is not the case for single-step chemistry. Moreover, the flame response depends on the flame-wall heat interaction, which changes with the flame stand-off distance. Single-step chemistry parameters need to be tuned to predict this stand-off distance accurately and this tuning needs to be adjusted for different operating conditions, as noted in chapter 3. From here on, I use the detailed kinetics mechanism for all the computations.

Comparing the adiabatic wall and the conductive wall cases in Fig. 4-1, it is seen that heat exchange with the wall is necessary for predicting larger than unity gain. Similar observations were made in previous analytical [1] and numerical [9] investigations. The gain is greater than unity when a positive feedback loop between

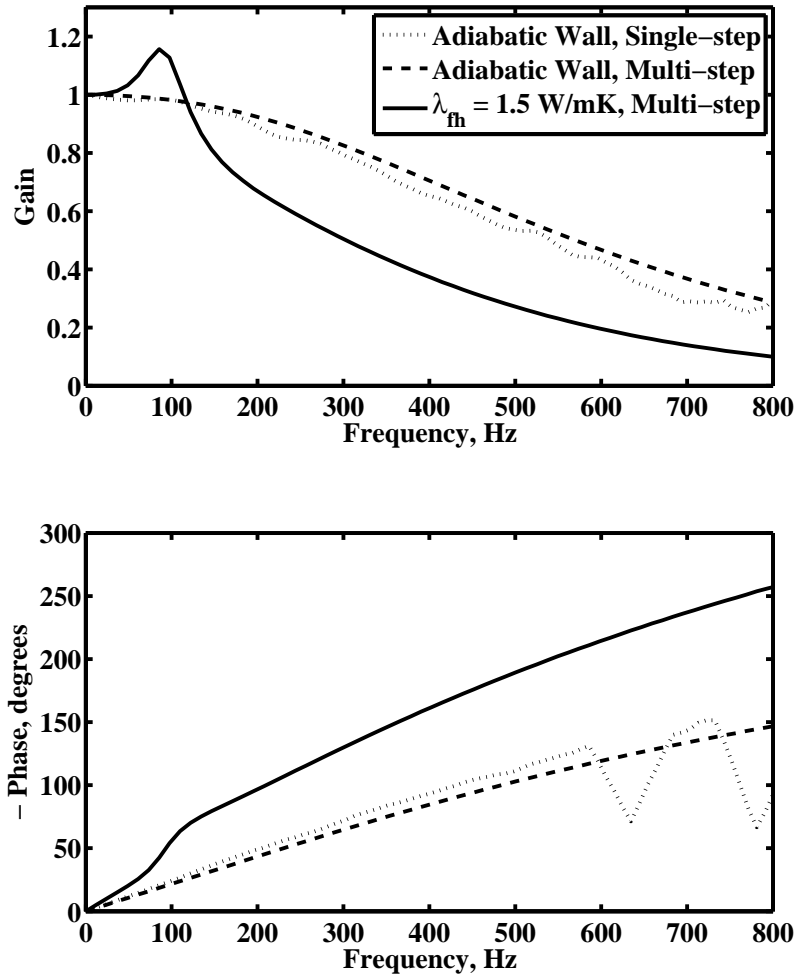


Figure 4-1: Linear flame response: Impact of kinetics mechanism and heat exchange with the plate surface, for constant $\phi = 0.75$, $\bar{u}_{in} = 0.8$ m/s, and $\kappa = 2R = 1$ mm on the total heat release rate, Q_f

the heat release rate and velocity perturbation is established. Heat exchange with the plate is the mechanism required for closing the feedback loop. When the flame is closer to the plate, the heat exchange rate rises, which decreases the burning velocity near the flame base. This increases the flame stand off distance which lowers the heat exchange and increases the burning velocity, establishing the feedback loop. It should be noted that this is observed for a weakly conducting plate, showing the sensitivity of the the flame response to the flame-wall heat exchange boundary conditions.

As noted by Fleifil et al. [17] and de Goey et al. [9], at higher frequencies, the gain drops rapidly, that is the flame behaves as a low pass filter. Consistent

with the previous studies, the phase plot (negative of the phase is shown) shows a delay in the flame response, with almost linear variation with frequency beyond the resonance condition. Experimental observations show similar linear growth of the phase delay with frequency, contrary to the theoretical analysis that predicts phase saturation near 90° [22]. I observe the same linear increase in the phase, and no phase saturation frequencies were seen within the range of operating conditions of the simulations. This is also contrary to the numerical predictions in [9]. A unity gain at low frequencies indicates that the heat release oscillations vary linearly with the velocity perturbations, with no damping or driving mechanisms at these frequencies. At high frequencies, the wavelength of the perturbations are small. Local changes resulting from small wavelength perturbations are damped out by the flame, resulting in diminishing gain [17]. The frequency response at higher frequency point to a time delay caused by the convection time needed by the reactants to reach the flame base, $\tau_\kappa \sim \delta/\bar{u}_{in}$, where δ is the flame stand-off distance above the plate. Increasing the inlet velocity raises the flame stand-off distance keeping τ_κ almost constant. The phase lag, $2\pi f\tau_\kappa$ (in radians), grows linearly with frequency as observed in Fig. 4-1. It must be noted that the frequency response is very sensitive to the heat loss.

The flame-wall interaction is a crucial mechanism which results in the resonant behavior observed in the larger-than unity gain. Figure 4-4 shows the transfer functions for the heat exchange at the top of the plate, Q_{top} , $S_{c,0}$, $S_{c,\kappa}$ and Q_f . This is obtained for the same conductive plate case shown in Fig. 4-1. Q_{top} is computed by integrating the heat flux entering the top plate surface across the surface in the cylindrical domain. At the resonant frequency, Q_{top} oscillations are very high. This provides a strong driving mechanism for the Q_f oscillations near the resonant frequency, resulting in the observed high gain. The resonant frequency is a strong function of the Q_{top} , which depends strongly on the flame stand-off distance and the plate conductivity, as noted in chapter 3. In the absence of the flame-wall interaction, $Q_{top} = 0$ and no resonance is seen. The phase difference between Q_f and $S_{c,\kappa}$ is nearly zero at all frequencies. This was observed across all parametric variations in the study, showing an interesting aspect of the flame response. Similar to Q_f , $S_{c,\kappa}$ lags the inlet velocity

perturbation by the convection time delay of the reactants, τ_κ , that is, the flame response is consistent with the response of its base. In previous studies, the time lag was attributed to the convective delay required by the reactants to reach the flame tip [9]. However, the results show that the extra delay in $S_{c,0}$ has a weaker impact on Q_f . Moreover, at higher frequencies, the phase of the flame-wall interaction saturates, further damping the heat release rate oscillations.

In Figs. 4-2 and 4-3, I use a base case to investigate the impact of the different operating parameters on the linear transfer function. The base case corresponds to $\lambda_{fh} = 1.5$ W/mK, $\phi = 0.75$, $\bar{u}_{in} = 1.3$ m/s, and $\kappa = 2R = 1$ mm. This corresponds to a Zeldovich number representative of the detailed mechanism, $Ze = \frac{E_a}{RT_b^2}(T_b - T_u)$ of $Ze = 10.7$ (assuming activation temperature $T_a = 24400$ K) and an inlet Reynolds number based on the maximum velocity and hole diameter of $Re = 162$. For the plate, the thickness ratio is $(L/D_p) = 13.2$ (where D_p is the difference between the outer and inner diameter of the plate). All the cases take into account the flame-wall interaction and detailed kinetics.

Figure 4-2 shows the impact of the mean inlet velocity and the distance between the adjacent holes on the linear flame response. The equivalence ratio and the plate thermal conductivity are kept constant. The qualitative observations of the gain and phase in the presence of flame-wall interaction remain the same as before. As the mean inlet velocity is decreased, the flame height and the flame stand-off distance are reduced, as seen in chapter 3. The low pass filter behavior of the flame becomes more prominent, i.e., higher oscillations are attenuated more rapidly. The flame-wall interaction is stronger when the flame is closer to the plate, and at higher frequency, this interaction acts as a damping mechanism, resulting in stronger attenuation. The phase lag has nearly the same slope because of the reduction in both the stand-off distance and the inlet velocity, keeping the time lag τ_κ almost the same. Increasing the distance between the adjacent flames decreases the volumetric heat release rate near the flame base because the flame wall interaction becomes stronger, as noted in chapter 3. The stand-off distance increases, which would have been expected to make time delay longer. However, this behavior is not seen. This is because of the

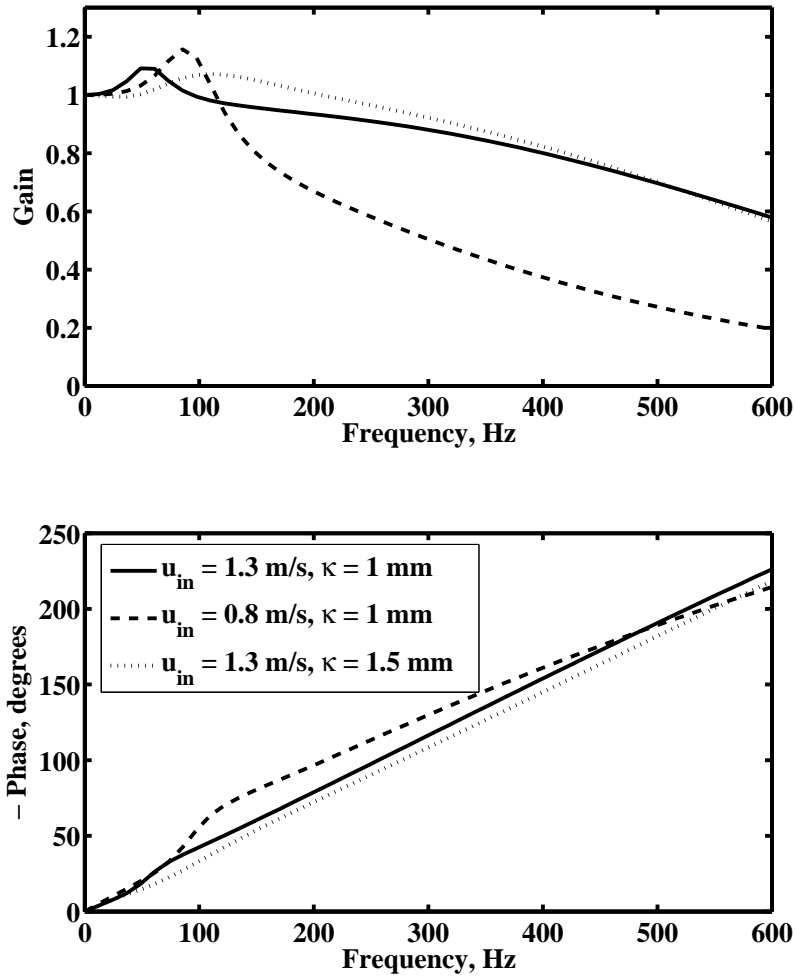


Figure 4-2: Linear flame response: Impact of the mean inlet velocity \bar{u}_{in} , and outer plate radius κ , for constant $\phi = 0.75$ and $\lambda_{fh} = 1.5$ W/mK on the total heat release rate, Q_f

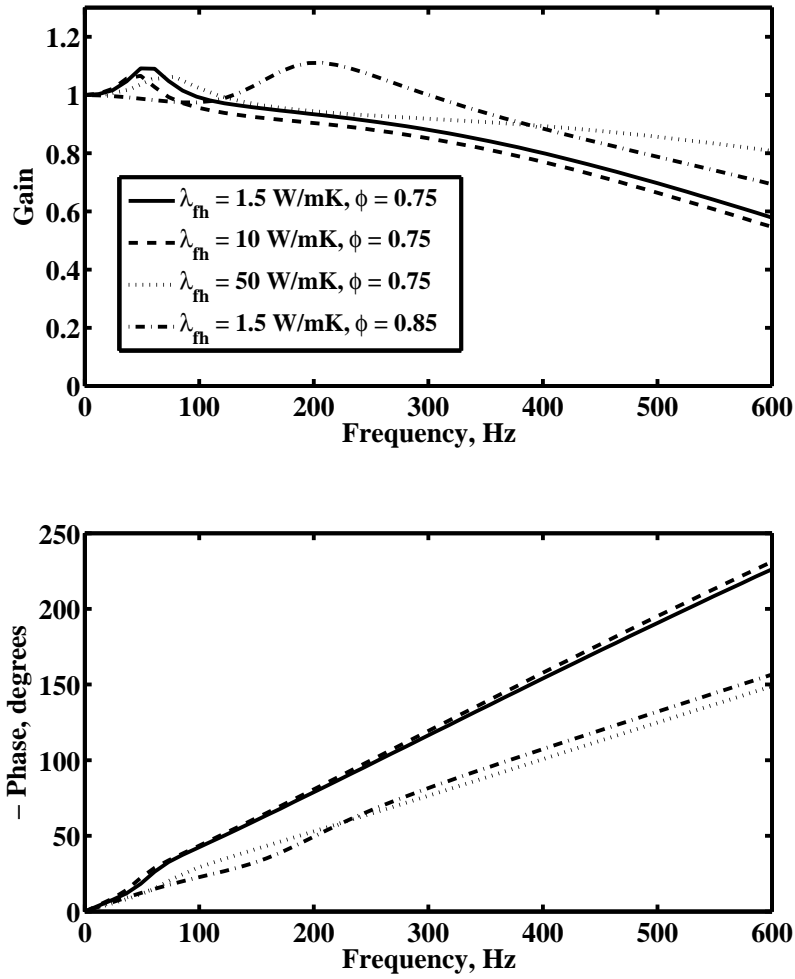


Figure 4-3: Linear flame response: Impact of the plate thermal conductivity λ_{fh} and equivalence ratio ϕ , for constant $\bar{u}_{in} = 1.3 \text{ m/s}$ and $\kappa = 1 \text{ mm}$ on the total heat release rate, Q_f

acceleration of the reactants due to the heat exchange between the hot plate and the cold reactants flowing inside the hole. The resonant frequency of the burner changes with \bar{u}_{in} and κ because the flame-wall interaction changes significantly.

Figure 4-3 shows the impact of the plate thermal conductivity and the equivalence ratio on the linear flame response. The mean inlet velocity and the distance between the adjacent holes are kept constant. Raising the equivalence ratio enhances the heat release rate resulting in higher maximum gain, while decreasing the flame stand-off distance. The convective time delay, τ_κ , becomes shorter decreasing the overall slope of the phase delay. The resonant frequency shifts considerably as the flame-wall interaction increases for $\phi = 0.85$. The slope of the gain curve is higher for $\phi = 0.85$, again indicating that stronger flame-wall interaction result in high damping at large frequencies. At higher thermal conductivity, the flame stand-off increases, eventually becoming constant, as noted in [32]. The phase delay also reaches a constant value at $\lambda = 10$ W/mK. But this is not true at very high plate conductivities because the heat lost to the plate top is transferred back into the reactants as they flow up the hole. Therefore, even if the stand-off distance saturates, reactants are accelerating because of higher heat flux from the hole resulting in higher convection velocity into the flame. Analytical efforts to incorporate the acceleration of the reactants into the time lag τ_κ are necessary in order to accurately model flame dynamics.

From the discussion of Fig. 4-4, it is clear that the flame response to perturbations is strongly impacted by the response of the flame base, where a strong flame-wall interaction is present. The convection delay between the inlet perturbations and the flame base results in a phase delay in the transfer functions. The convection time delay, τ_κ , does not solely depend on the flame stand-off distance and the inlet velocity. The heat transfer to the top surface of the plate is fed back to the reactants from the sides of the hole, accelerating the flow and decreasing the convective time delay. Flame-wall interaction is critical in closing the feedback loop between heat release rate and velocity oscillations which leads to the observed resonance at low frequency. This has not been investigated fully in previous studies and the new insight should be incorporated in the analytical models developed to predict the

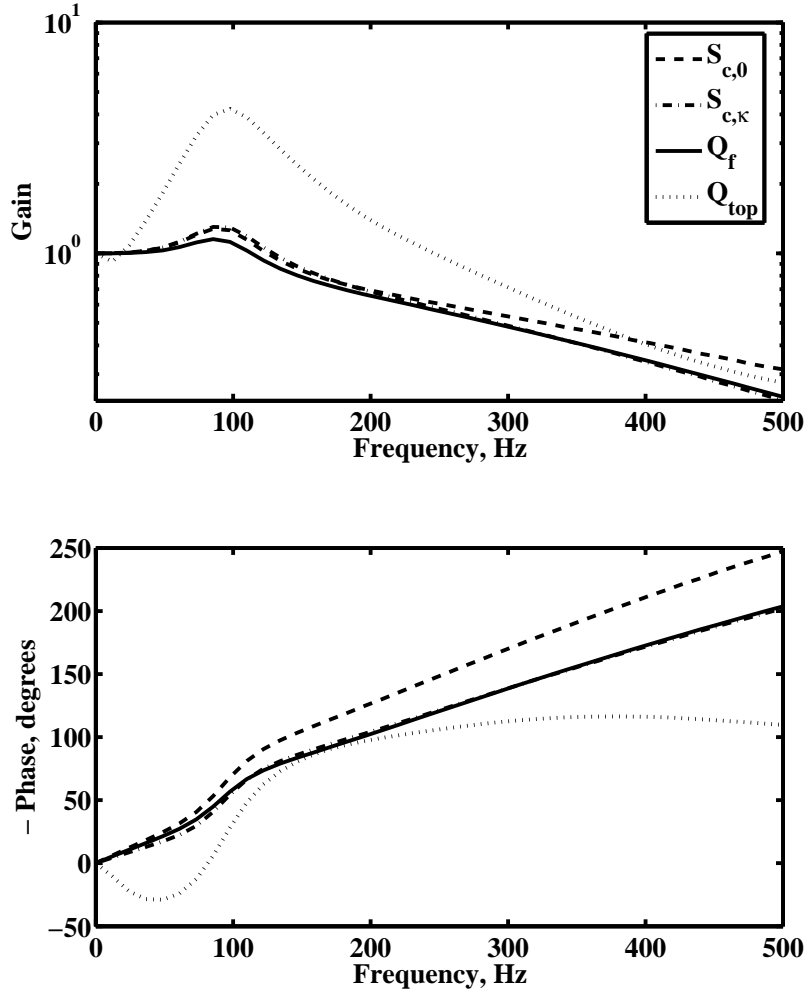


Figure 4-4: Linear response of the heat exchange at the top surface of the plate, Q_{top} , $S_{c,0}$, $S_{c,\kappa}$ and the total heat release rate, Q_f , for $\lambda_f = 1.5$ W/mK, $\phi = 0.75$, $\bar{u}_{in} = 0.8$ m/s, and $\kappa = 2R = 1$ mm

flame transfer functions.

4.2 Time Domain Analysis

The steady-state solution for a given set of operating conditions is used as the initial solution for analyzing large amplitude oscillations in the time domain. The base case, described above, is analyzed in this section, with a sinusoidal inlet velocity forcing. Results are used to shed more light on the flame response to inlet velocity oscillations.

Figure 4-5 shows a cycle of Q_f , \bar{u}_{in} , flame surface area, A_f and Q_{top} , at an inlet

velocity forcing with $A = 0.4$, $f = 50$ Hz and $A = 0.4$, $f = 250$ Hz. All quantities are non-dimensionalized with respect to the mean quantities computed using the steady-state solution. A_f is computed using the maximum volumetric heat release rate contour. Similar to the linear response discussed in Section 4.1, Q_f oscillations lag \bar{u}_{in} oscillations for both the cases, with higher lag for $f = 250$ Hz. The oscillations in A_f and Q_{top} significantly contribute to the Q_f oscillations. Flame surface area oscillations are in phase with Q_f . At the higher frequency, the Q_{top} oscillation is weaker, indicating that most of the heat release fluctuations are a result of the flame surface area oscillations. As the frequency increases, the phase between A_f and Q_f remains almost the same, but the phase between Q_{top} and Q_f changes confirming the role of heat exchange in the dynamic mechanism.

Figure 4-6 shows a cycle of \bar{u}_{in} , Q_{top} , $S_{c,0}$ and $S_{c,\kappa}$, at a velocity forcing with $A = 0.4$, $f = 50$ Hz and $A = 0.4$, $f = 250$ Hz. The impact of the flame-wall interaction can best be seen from the flame consumption speeds $S_{c,0}$ and $S_{c,\kappa}$. As the flame wall-interaction becomes stronger (maximum Q_{top} amplitude), $S_{c,\kappa}$ reaches a minimum because the reduction in the flame stand-off distance. This inverse relationship is noted in chapter 3 for steady flames. At higher frequency, this direct impact of Q_{top} on $S_{c,\kappa}$ remains the same, further ascertaining that the flame response is strongly impacted by the dynamics at the flame base. $S_{c,0}$ lags $S_{c,\kappa}$ because of additional convective delay as the perturbations travel along the axis towards the flame tip. At higher frequency, the phase lag between $S_{c,0}$ lags $S_{c,\kappa}$ increases.

To visualize the mechanisms impacting the flame dynamics, Fig. 4-7 shows the instantaneous contours of the volumetric heat release rate at different instances in the cycle with inlet velocity forcing at $A = 0.4$, $f = 50$ Hz, superimposed on a 2D velocity map. As the flame moves away from the plate, its area and volumetric heat release rates grow, resulting in higher Q_f and higher $S_{c,\kappa}$. The flame-wall interaction is weaker during this time, as seen in Fig. 4-5 where the Q_{top} and Q_f are almost out of phase. As the flame moves closer, back towards the plate, its volumetric heat release rate, and hence $S_{c,\kappa}$, are reduced because of the stronger flame-wall interaction.

Higher amplitude perturbations lead to flame steepening because of the rise of

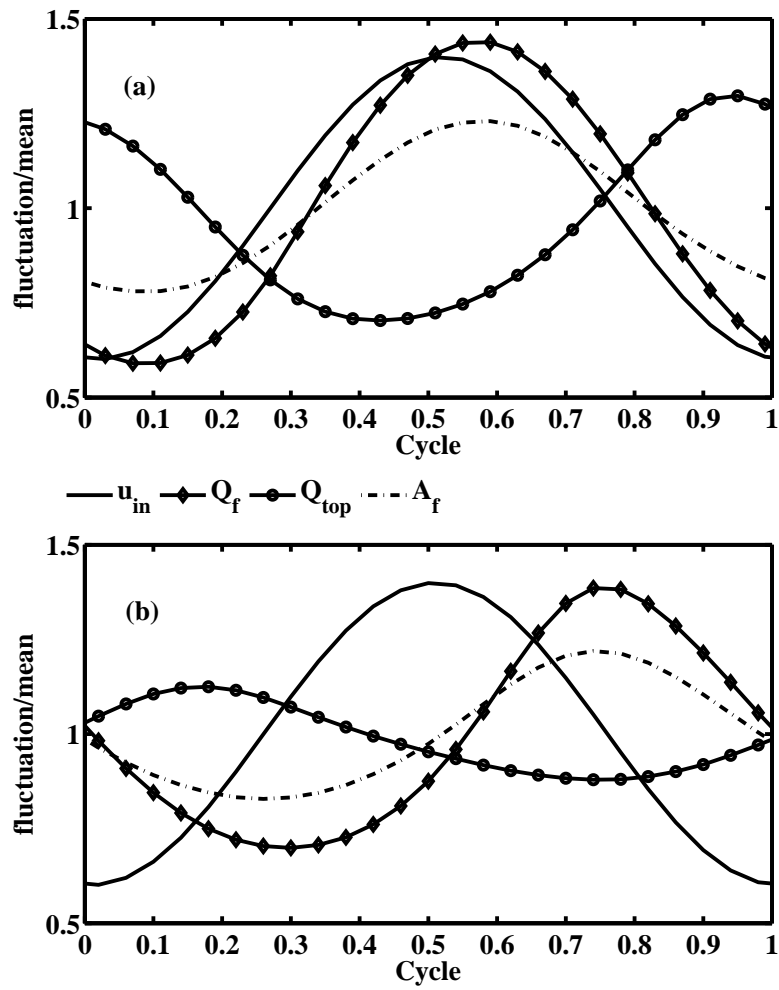


Figure 4-5: A cycle of Q_f , \bar{u}_{in} , flame area, A_f and Q_{top} for the base case ($\phi = 0.75$, $\lambda_{fh} = 1.5$ W/mK, $\bar{u}_{in} = 1.3$ m/s, $\kappa = 1$ mm) with $A = 0.4$; (a) $f = 50$ Hz and (b) $f = 250$ Hz

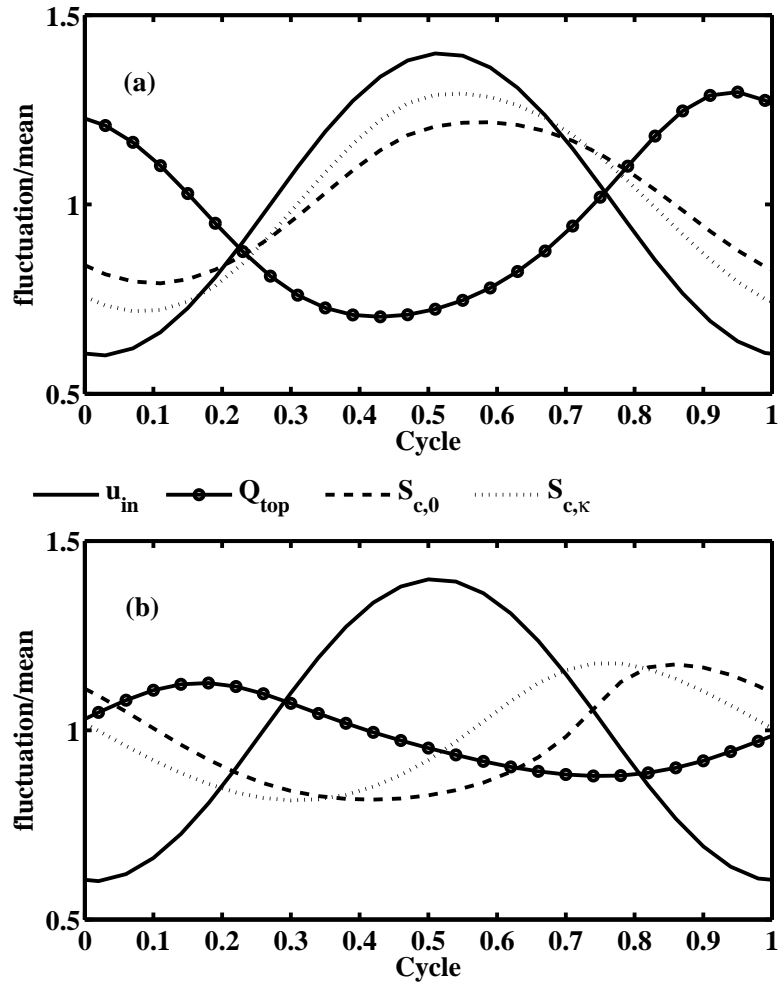


Figure 4-6: A cycle of \bar{u}_{in} , $S_{c,0}$, $S_{c,\kappa}$, and Q_{top} for the base case ($\phi = 0.75$, $\lambda_{fh} = 1.5$ W/mK, $\bar{u}_{in} = 1.3$ m/s, $\kappa = 1$ mm) with $A = 0.4$; (a) $f = 50$ Hz and (b) $f = 250$ Hz

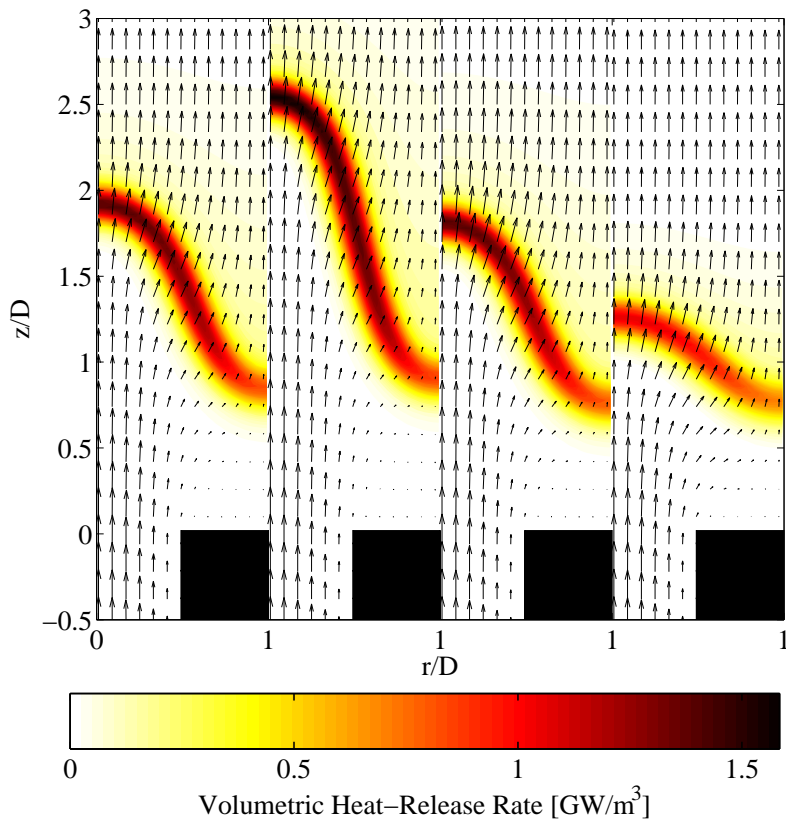


Figure 4-7: Velocity vectors and volumetric heat release rate contours at different instances of the inlet velocity forcing cycle, with $A = 0.4$, $f = 50$ Hz, $\phi = 0.75$, $\lambda_{fh} = 1.5$ W/mK, $\bar{u}_{in} = 1.3$ m/s, $\kappa = 1$ mm

higher harmonics. This further impacts the flame response to velocity perturbations, which cannot be analyzed using linear transfer function techniques. Time domain simulations should be used, alongwith the frequency domain results, to further investigate these phenomena. Nonlinear response and the impact of the flame-wall interaction will be investigated in the future.

4.3 Conclusions

In this chapter, the flame response to imposed velocity perturbations over a certain range of design and operating conditions using two-dimensional simulations of perforated-plate stabilized premixed, laminar methane-air flames with detailed chemical kinetics is investigated. Linear flame transfer functions were obtained using Fourier analysis of the flame response data to a small amplitude sudden impulse in the inlet velocity. Time domain analysis of the flame response to a sinusoidal velocity forcing was also analyzed.

The results show that the flame-wall interaction is crucial in closing the feedback loop between the heat release rate and the velocity oscillations. This may result in a resonant behavior in perforated-plate stabilized burners. Conductive walls increase/decrease the gain at low/high frequencies as compared to adiabatic walls. The flame stand-off distance oscillations caused by the convection as well as the flame-wall interaction impacts the dynamics significantly because it determines the heat flux to the wall. The flame response to perturbations originates near the flame base in the form of the burning velocity oscillations. The phase lag between heat release rate and the velocity oscillations is governed by the convection of the reactants into the flame base region. This convective delay depends on the flame stand-off distance and the acceleration of the reactants as the heat circulates from the top plate to the side walls of the holes. The additional convective delay between the perturbations at the flame base and the flame tip has a weaker impact on the flame response. At higher frequency, flame-wall interaction is weaker and heat release rate oscillations are a result of the flame area oscillations.

Chapter 5

Summary and Future Work

5.1 Summary

A two-dimensional reactive flow solver is developed using high-efficiency numerical implementations. Steady and unsteady characteristics of perforated-plate stabilized laminar premixed flames are analyzed using a detailed chemical kinetics mechanism. Conventional reactive flow solvers are generally very expensive, making simulations with detailed chemical kinetics infeasible. High-efficiency parallel algorithms, which are typically hybrid of conventional schemes, can improve the performance of reactive flow codes by huge factors, as reported in Chapter 2. The combustion problem, numerically investigated in this thesis, has previously been analyzed by researchers. One or more approximations such as one-dimensional formulation, flat flame approximation, single-step chemistry have been used in analytical studies, because of the complex nature of the problem, as well as in numerical analysis because of the limited computational resources. However, high-efficiency numerical implementations along with the continuously increasing computing power can be exploited to analyze combustion phenomena more accurately, and predict their dynamics quantitatively and qualitatively. This has been demonstrated in this work.

Our predictions show that the plate thermal conductivity and distance between the neighboring holes (often termed as the plate porosity) are important design parameters of perforated-plate stabilized burners. The mean inlet velocity and equivalence

ratio are important reactant mixture parameters. These parameters determine the characteristics of the premixed flame stabilized on such burners. The impact on the flame height, flame stand-off distance, flame consumption speeds and burner plate temperature are reported in Section 3.6. In the presence of heat communication with the plate, the flame stabilizes on the top of the perforated-plate instead of being attached as in the case of an adiabatic plate. The flame is curved both at its thin tip and near its thick base. The flame base region is much thicker than the typically observed thin reaction fronts in premixed flames, as seen near the flame tip and as seen in the case of the flame in the presence of an adiabatic wall. This suggests that significantly different transport processes govern the stability of the flame base compared to that of the flame tip. The net heat loss to the surface of the perforated plate and the temperature of the perforated plate are crucial physical quantities that impact the design decisions of such burners. Our numerical tool can be used to predict these quantities avoiding expensive experimental analysis. The steady flame results can be used to gain insight into the dominant physical processes in such a burner configuration. Using these results, an analytical model can potentially be developed, capturing most of the physics in a reduced form.

The impact of the parameters on the transfer function characteristics of such burners are analyzed in Chapter 4. The non-dimensional gain is greater than unity in the low frequency regime, in the case of a conducting burner plate. This gain drops rapidly at higher frequencies. It is concluded, in Section 4.3, that the flame-wall interaction is a crucial mechanism impacting the unsteady flame response to inlet velocity oscillations. The convection of the reactants into the flame base determine the phase lag in the transfer functions. The heat conducting burner plate provides an energy feedback mechanism towards the reactants, impacting the dynamic behavior of the flame. The transfer functions establishes a thermo-kinetic relation between the flame and the flow via the heat exchange mechanism with the perforated-plate. This relation can be further exploited for thermoacoustic investigations.

5.2 Suggested Future Work

The work reported in this thesis can be used as a base for extending the scope of the problem and further improve our understanding of perforated-plate burners, which are heavily used in practical applications. Few possible extensions are mentioned in this section.

The SplitStiff numerical scheme demonstrates high performance of a reactive flow solver. Although significantly faster than other schemes, the current implementation has two major limitations (i) The utilization of OpenMP for parallelization (ii) The use of a uniform grid. Development of a MPI implementation will make it possible to scale the solver to a very large number of processors resulting in significant speed ups. Non-uniform structured grids, with a fine mesh near the flame and coarse mesh away from the flame will reduce the computational cost significantly. This however would require adaptive meshing inside the solver as the flame may move in intermediate solutions, making the code development complex. Both these features can boost up the code performance significantly and must be considered while writing a new reactive flow solver or extending the extending solver. Further modularity should be added in a new code which can generalize its use to different combustion problems in two-dimensions and is geometrically flexible.

The complex physics near the stagnation region should be investigated in the case of steady flames, to understand the observations reported near the flame base, in further detail. The numerical results must be carefully analyzed to understand the underlying physical mechanism and embed them in an analytical model that can capture the physics. This analysis can potentially give a qualitative insight into similar problems in combustion such has the interaction between a flame and solid particles in a heterogeneous flow, in the presence of heat exchange, etc.. Strong curvatures are seen both near the flame tip and the flame base. The impact of this on the burning velocity oscillations must be studied. The physical mechanisms governing the static stability of the flame tip must be differentiated from those of the flame base. Radiation is ignored in the current work, although it may have significant

impact on the results. Radiative heat losses are volumetric which can alter the dynamic characteristics of the premixed flame on the perforated-plate. Thus, radiation must be modeled in future analysis. The current work is limited to aspect ratios such that the fully developed momentum and velocity profiles assumptions are valid. To relax this limitation, an elaborate treatment of inflow boundary conditions for studying small aspect ratio domains and high bottom wall convective heat transfer coefficients needs to be considered.

Further detailed investigation of the flame-wall interaction is warranted because of its significant role in the flame dynamics mechanism. The greater than unity gain in the transfer functions show that there exists a selective unsteady mechanism in the problem, which must be isolated and investigated. This mechanism can potentially lead to the onset of self-sustained combustion oscillations, different from the self-sustained thermo-acoustic oscillations. The onset of such combustion oscillations because of the heat losses to the wall were reported in edge-flames by Matalon [27]. Di Sarli et. al. [39] emphasize the impact of the thermo-kinetic interaction (flame-wall interaction) on spontaneous oscillations. Similar unsteady studies with the perforated plate configuration can be attempted to further improve our understanding of flames in such systems. Results of such studies must be embedded in analytical models for designing perforated plate flame holder with superior stability characteristics. The analytical model can then be used in performing thermo-acoustic instability analysis of these burners. The transfer function analysis carried out in this thesis is in the linear regime. Nonlinear response of the heat release rate to inlet velocity oscillations is also an important possible extension to the problem.

Bibliography

- [1] H. M. Altay, S. Park, D. Wu, D. Wee, A. M. Annaswamy, and A. F. Ghoniem. Modeling the dynamic response of a laminar perforated-plate stabilized flame. *Proc. Combust. Inst.*, 32:1359–1366, 2009.
- [2] B. Bennett, C. S. Mcenally, L. D. Pfefferle, and M. D. Smooke. Computational and experimental study of axisymmetric coflow partially premixed methane/air flames. *Combustion and Flame*, 123:522–546, 2000.
- [3] P. N. Brown, G. D. Byrne, and A. C. Hindmarsh. Vode: a variable-coefficient ode solver. *SIAM Journal of Scientific Computing*, 10(5):1039–1051, 1989.
- [4] S. Candel. Combustion dynamics and control: Progress and challenges. *Proc. Combust. Inst.*, 29:1–28, 2002.
- [5] S. H. Chung and C. K. Law. An invariant derivation of flame stretch. *Combustion and Flame*, 55:123–125, 1984.
- [6] P. Clavin. Premixed combustion and gas dynamics. *Annu. Rev. Fluid Mech.*, 26:321–352, 1994.
- [7] J. Daou and M. Matalon. Influence of conductive heat-losses on the propagation of premixed flames in channels. *Combustion and Flame*, 128:321–339, 2002.
- [8] L. P. H. de Goey and H. C. de Lange. Flame cooling by a burner wall. *Int. J. Heat and Mass Transfer*, 37:635–646, 1994.
- [9] P. de Goey, V. Kornilov, R. Rook, and J. Ten Thije Boonkamp. Experimental and numerical investigation of the acoustic response of multi-slit bunsen burners. In *155th Meeting of the Acoustical Society of America*. AIAA, 2008. Acoustics’08 Paris.
- [10] H. C. de Lange and L. P. H. de Goey. Two-dimensional methane/air flame. *Combustion Science and Technology*, 92:423–427, 1993.
- [11] H. C. de Lange and L. P. H. de Goey. Numerical flow modeling in a locally refined grid. *Int. J. Num. Meth. in Eng.*, 37:497–515, 1994.
- [12] S. Ducruix, D. Durox, and S. Candel. Theoretical and experimental determinations of the transfer function of a laminar premixed flame. *Proc. Combust. Inst.*, 28:765–773, 2000.

- [13] S. Ducruix, T. Schuller, D. Durox, and S. Candel. Combustion dynamics and instabilities: Elementary coupling and driving mechanisms. *Journal of Propulsion and Power*, 19(5):722–733, 2003.
- [14] D. Durox, T. Schuller, N. Noiray, and S. Candel. Experimental analysis of nonlinear flame transfer functions for different flame geometries. *Proc. Combust. Inst.*, 32:1391–1398, 2009.
- [15] T. Echekki and J. H. Ferziger. Studies of curvature effects on laminar premixed flames: Stationary cylindrical flames. *Combustion Science and Technology*, 90:231–252, 1993.
- [16] A. Ern, C. C. Douglas, and M. D. Smooke. Detailed chemistry modeling of laminar diffusion flames on parallel computers. *International Journal of Supercomputer Applications and High Performance Computing*, 9:167–186, 1995.
- [17] M. Fleifil, A. M. Annaswamy, Z. A. Ghoneim, and A. F. Ghoniem. Response of a laminar premixed flame to flow oscillations: A kinematic model and thermoacoustic instability results. *Combustion and Flame*, 106(4):487–510, 1996.
- [18] D. G. Goodwin. Cantera: object-oriented software for reacting flows. <http://www.cantera.org>.
- [19] Robert J. Kee, Michael E. Coltrin, and Peter Glarborg. *Chemically reacting flow: theory and practice*. John Wiley and Sons, Inc., 2003.
- [20] N. Kim and K. Maruta. A numerical study on propagation of premixed flames in small tubes. *Combustion and Flame*, 146:283–301, 2006.
- [21] O. M. Knio, H. N. Najm, and P. S. Wyckoff. A semi-implicit numerical scheme for reacting flow, ii. stiff, operator-split formulation. *Journal of Computational Physics*, 154:428–467, 1999.
- [22] V. Kornilov, K.R.A.M. Schreel, and L.P.H. de Goeij. Experimental assessment of the acoustic response of laminar premixed bunsen flames. *Proc. Combust. Inst.*, 31:1239–1246, 2007.
- [23] S. T. Lee and C. H. Tsai. Numerical investigation of steady laminar flame propagation in a circular tube. *Combustion and Flame*, 99:484–490, 1994.
- [24] T. Lieuwen. Modeling premixed combustion-acoustic wave interactions: A review. *Journal of Propulsion and Power*, 19(5):765–781, 2003.
- [25] R. M. M. Mallens, H. C. de Lange, C. H. J. van de Ven, and L. P. H. de Goeij. Modeling of confined and unconfined laminar premixed flames on slit and tube burners. *Combustion Science and Technology*, 107:387–401, 1995.
- [26] Y. M. Marzouk, A. F. Ghoniem, and H. N. Najm. Toward a flame embedding model for turbulent combustion simulation. *AIAA Journal*, 41(4):641–652, 2003.

- [27] M. Matalon. Flame dynamics. *Proc. Combust. Inst.*, 32:57–82, 2009.
- [28] A. C. McIntosh. On the cellular instability of flames near porous-plug burners. *Journal of Fluid Mechanics*, 161:43–75, 1985.
- [29] A. C. McIntosh. On the effect of upstream acoustic forcing and feedback on the stability and resonance behavior of anchored flames. *Combustion Science and Technology*, 49(3-4):143–167, 1986.
- [30] A. C. McIntosh. Combustion-acoustic interaction of a flat flame burner system, enclosed within an open tube. *Combustion Science and Technology*, 54(1-6):217–236, 1987.
- [31] A. C. McIntosh and J. F. Clarke. 2nd order theory of unsteady burner-anchored flames with arbitrary lewis number. *Combustion Science and Technology*, 38(3-4):161–196, 1984.
- [32] A. C. McIntosh and J. F. Clarke. A review of theories currently being used to model steady plane flames on flame-holders. *Combustion Science and Technology*, 37(3-4):201–219, 1984.
- [33] P. G. Mehta, M. C. Soteriou, and A. Banaszuk. Impact of exothermicity on steady and linearized response of a premixed ducted flame. *Combustion and Flame*, 141(4):392–405, 2005.
- [34] H. N. Najm and P. S. Wyckoff. Premixed flame response to unsteady strain rate and curvature. *Combustion and Flame*, 110:92–112, 1997.
- [35] H. N. Najm, P. S. Wyckoff, and O. M. Knio. A semi-implicit numerical scheme for reacting flow, i. stiff chemistry. *Journal of Computational Physics*, 143:381–402, 1998.
- [36] M. V. Petrova and F. A. Williams. A small detailed chemical-kinetic mechanism for hydrocarbon combustion. *Combustion and Flame*, 144:526–544, 2006.
- [37] R. Rook. *Acoustics in Burner Stabilized Flames*. PhD thesis, Eindhoven University of Technology, Eindhoven, The Netherlands, <http://www.tue.nl/bib/>, 2001.
- [38] R. Rook, L. P. H. de Goeij, L. M. T. Somers, K. R. A. M. Schreel, and R. Parchen. Response of burner-stabilized flat flames to acoustic perturbation. *Combustion Theory and Modeling*, 6:223–242, 2002.
- [39] V. Di Sarli, F. S. Marra, and A. Di Benedetto. Spontaneous oscillations in lean premixed combustors: Cfd simulation. *Combustion Science and Technology*, 179:2335–2359, 2007.
- [40] K. R. A. M. Schreel, R. Rook, and L. P. H. de Goeij. The acoustic response of burner-stabilized flat flames. *Proc. Combust. Inst.*, 29:115–122, 2002.

- [41] T. Schuller, S. Ducruix, D. Durox, and S. Candel. Modelling tools for the prediction of premixed flame transfer functions. *Proc. Combust. Inst.*, 29:107–113, 2002.
- [42] T. Schuller, D. Durox, and S. Candel. A unified model for the prediction of laminar flame transfer functions: comparisons between conical and v-flame dynamics. *Combustion and Flame*, 134:21–34, 2003.
- [43] G. P. Smith, D. M. Golden, M. Frenklach, N. W. Moriarty, B. Eiteneer, M. Goldenberg, C. T. Bowman, R. K. Hanson, S. Song, Jr. W. C. Gardiner, V. V. Lissianski, and Z. Qin. Gri-mech 3.0. http://www.me.berkeley.edu/gri_mech/.
- [44] Z. B. Song, L. J. Wei, and Z. Z. Wu. Effects of heat losses on flame shape and quenching of premixed flames in narrow channels. *Combustion Science and Technology*, 180:264–278, 2008.
- [45] R. L. Speth, Y. M. Marzouk, and A. F. Ghoniem. Impact of hydrogen addition on flame response to stretch and curvature. In *43rd Aerospace Sciences Meeting*. AIAA, 2005. AIAA-2005-143.
- [46] C. K. Westbrook and F. L. Dryer. Simplified reaction mechanisms for the oxidation of hydrocarbon fuels in flames. *Combustion Science and Technology*, 27:31–43, 1981.

List of Publications Based on this Thesis

1. Altay H. M., Kedia, K. S., Speth, R. L. and Ghoniem, A. F., Two-Dimensional Simulations of Steady Perforated-Plate Stabilized Premixed Flames. *Combustion Theory and Modelling*, Volume 14, pp. 125-154, 2010.
2. Kedia, K. S., Altay H. M. and Ghoniem, A. F., Impact of Flame-Wall Interaction on Flame Dynamics and Transfer Function Characteristics. *33rd International Symposium on Combustion*, Beijing, China, August 2010.
3. Altay H. M., Kedia, K. S., Speth, R. L. and Ghoniem, A. F., Simulations of Laminar Perforated-Plate Stabilized Flame Dynamics. *6th U.S. National Combustion Meeting*, Ann Arbor, Michigan, U.S.A., May 2009.